GEOSPLATTING: TOWARDS GEOMETRY GUIDED GAUSSIAN SPLATTING FOR PHYSICALLY-BASED INVERSE RENDERING

Anonymous authors
Paper under double-blind review

ABSTRACT

We consider the problem of physically-based inverse rendering using 3D Gaussian Splatting (3DGS) representations (Kerbl et al., 2023b). While recent 3DGS methods have achieved remarkable results in novel view synthesis (NVS), accurately capturing high-fidelity geometry, physically interpretable materials and lighting remains challenging, as it requires precise geometry modeling to provide accurate surface normals, along with physically-based rendering (PBR) techniques to ensure correct material and lighting disentanglement. Previous 3DGS methods resort to approximating surface normals but often struggle with noisy local geometry, leading to inaccurate normal estimation and suboptimal material-lighting decomposition. In this paper, we introduce GeoSplatting, a novel hybrid representation that augments 3DGS with explicit geometric guidance and differentiable PBR equations. Specifically, we bridge isosurface and 3DGS together, where we first extract isosurface mesh from a scalar field, then convert it into 3DGS points and formulate PBR equations for them in a fully differentiable manner. In GeoSplatting, 3DGS is grounded on the mesh geometry, enabling precise surface normal modeling, which facilitates the use of PBR frameworks for material decomposition. This approach further maintains the efficiency and quality of NVS from 3DGS while ensuring accurate geometry from the isosurface. Comprehensive evaluations across diverse datasets demonstrate the superiority of GeoSplatting, consistently outperforming existing methods both quantitatively and qualitatively.

1 INTRODUCTION

The inverse rendering task, *i.e.*, recovering 3D attributes such as geometry, spatially-varying materials, and lighting from multi-view images or videos, has been a long-standing goal in computer vision and graphics. It plays a critical role in numerous industrial applications, including film production, gaming, and VR/AR, for photo-realistic novel-view synthesis and immersive user interactions. This task is typically approached using carefully designed 3D representations (Mildenhall et al., 2020; Müller et al., 2022; Wang et al., 2021; Shen et al., 2021; 2023) coupled with the corresponding differentiable rendering techniques (Boss et al., 2021a; Verbin et al., 2022a; Chen et al., 2019; Laine et al., 2020). While great progress has been made recently (Munkberg et al., 2022; Jiang et al., 2023; Gao et al., 2023), efficiently and accurately capturing various 3D attributes remains challenging due to the complexities of light transport in real-world environments, including intricate local geometry, non-Lambertian surface, complex lighting conditions, occlusions, *etc*.

The key to tackling the inverse rendering task lies in effectively modeling the underlying 3D geometry, where Physically-Based Rendering (PBR) techniques can be applied to disentangle materials and lighting. Numerous prior works have developed various 3D representations and their corresponding differentiable rendering equations to address this challenge, each offering unique advantages and limitations. Implicit representations (*e.g.*, NeRF (Mildenhall et al., 2020; Verbin et al., 2022b)) are well-suited for novel view synthesis but are computationally expensive and incompatible with existing graphics pipelines. In contrast, explicit representations (*e.g.*, mesh (Munkberg et al., 2022)) provide explicit geometry, allowing for well-defined rendering techniques, and facilitating tasks like relighting and material editing. However, optimizing explicit representations is challenging, especially when dealing with complex geometries like thin structures. More recently, 3D Gaussian Splatting (3DGS) (Kerbl et al., 2023b) has emerged as an efficient 3D representation

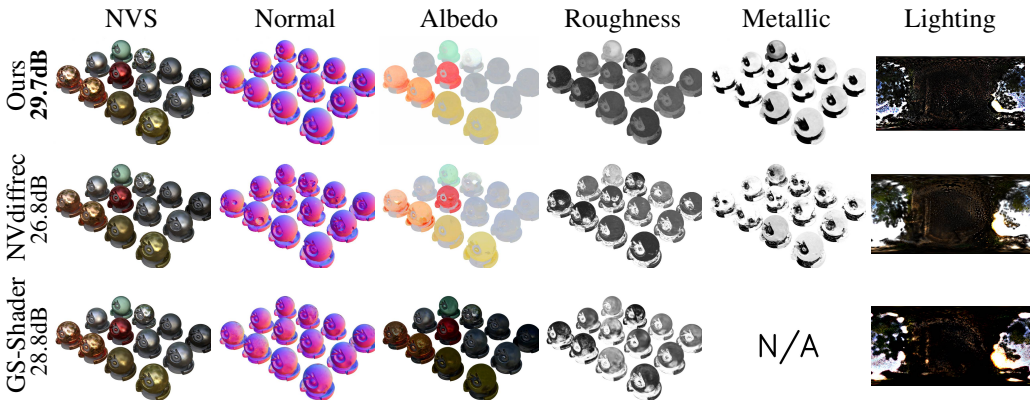

Figure 1: We propose GeoSplatting, a novel inverse rendering approach that augments Gaussian Splatting with explicit geometric guidance. GeoSplatting enables more accurate geometry recovery, and PBR material and lighting decomposition, achieving state-of-the-art performance in novel view synthesis. Note that our method and NVdiffrec (Munkberg et al., 2022) both adopt standard split-sum PBR model, while GS-Shader (Jiang et al., 2023) uses a modified version where albedo entangles with lighting. Please zoom in for details.

for high-quality novel-view synthesis. However, vanilla 3DGS is not designed to provide accurate geometry or disentangled materials, limiting its applicability to inverse rendering tasks. To tackle this challenge, various methods have studied assigning a normal direction to each 3DGS point to model local geometric surfaces, along with a PBR formula using the approximated normals (Jiang et al., 2023; Shi et al., 2023; Gao et al., 2023). However, these approaches offer only approximations of true normals, and as a result, may struggle with local minima in regions of complex geometry.

In this paper, we propose GeoSplatting, a more principled solution that leverages the strengths of both explicit representations and 3DGS for the inverse rendering task. At the core of GeoSplatting is a differentiable adaptor that integrates differentiable isosurface techniques (Shen et al., 2021; 2023) with 3D Gaussian Splatting. Specifically, we first utilize the differentiable isosurface techniques to extract a mesh from a scalar field that we want to optimize. We then introduce MGadapter, *i.e.*, Mesh-to-Gaussian-adaptor, that samples 3D Gaussian points on the mesh surface in a differentiable manner, naturally grounding the location of each Gaussian point on the surface geometry, from which we could estimate precise normal for each point. To render the sampled 3D Gaussian points, we design an efficient and differentiable PBR framework, leveraging the split-sum model (Karis, 2013) and applying it to the 3D Gaussian points. During training, since all the operations are differentiable, we can train our model end-to-end.

Our GeoSplatting offers several advantages over both 3DGS and explicit mesh-based representations. Compared to the vanilla 3DGS (Kerbl et al., 2023b) and its variants, our approach provides explicit geometric guidance from the isosurface, enabling more accurate normal estimation, which is crucial for inverse rendering optimization. On the other hand, compared to the mesh representations (Munkberg et al., 2022), GeoSplatting leverages the high efficiency and superior rendering quality inherited from 3DGS. Moreover, while the concept of constraining 3DGS with geometry is not new (Yu et al., 2024; Xiang et al., 2024), existing methods typically rely on a discrete optimization strategy where the implicit SDF field (Wang et al., 2021) and Gaussian points are learned separately. In contrast, GeoSplatting explicitly guides Gaussian points with the isosurface and can be optimized in an end-to-end fashion, reducing training time and improving the inverse rendering quality.

We conduct extensive experiments to demonstrate the effectiveness of our method, where GeoSplatting achieves new state-of-the-art training efficiency and inverse rendering performance on both the NeRF dataset and the DTU real-world dataset. We showcase that GeoSplatting exhibits improved geometry, more precise material and lighting disentanglement, and superior novel view synthesis compared to previous Gaussian Splatting baselines.

2 Related Work

3D Reconstruction Early works for 3D reconstruction primarily utilized structure-from-motion techniques to recover geometry, *i.e.*, estimating sparse or dense colored point clouds (Schonberger & Frahm, 2016; Fisher et al., 2021). Later, Neural Radiance Field (NeRF) (Mildenhall et al., 2020) represented scenes using implicit functions and leveraged differentiable volume rendering (Drebin

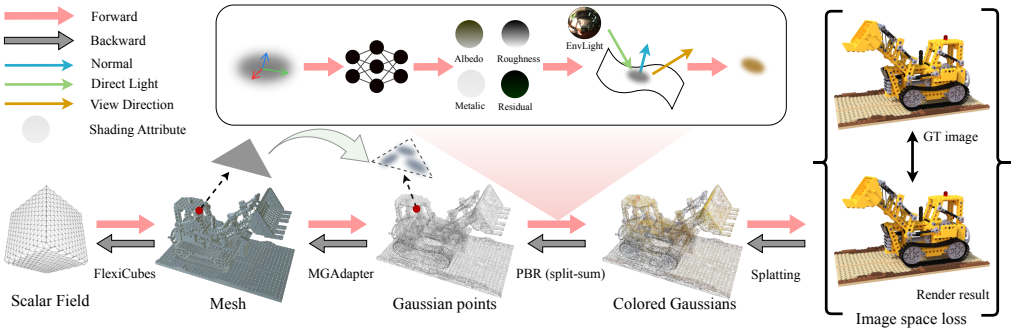

Figure 2: **Pipeline**. GeoSplatting first extracts an intermediate mesh from the scalar field, upon which Gaussian points are sampled and rendered using PBR equations. Finally, they are composited into images through the Gaussian rasterization pipeline. The entire process is fully differentiable.

et al., 1988) to reconstruct geometry and radiance, achieving highly detailed novel view synthesis. While NeRF encodes BRDF in a single radiance field, subsequent work has extended it by enhancing both the representations and the rendering equations to introduce more physical constraints, allowing the separation of physically-based rendering attributes such as normals, materials, and lighting (Verbin et al., 2022a; Boss et al., 2021a;b; Yariv et al., 2021; Wang et al., 2021; Zhang et al., 2021a; Liang et al., 2023; Ge et al., 2023). However, the use of implicit representations and volume rendering in these methods makes them difficult to integrate into existing graphics pipelines, as well as requires dense sampling that leads to slow rendering speed (Müller et al., 2022). On the other hand, explicit representations (*e.g.*, mesh (Shen et al., 2021; 2023)) combined with differentiable rendering techniques (Chen et al., 2019; 2021; Laine et al., 2020) have demonstrated their ability to extract explicit geometry, material, and lighting from multi-view images (Munkberg et al., 2022; Hasselgren et al., 2022). These approaches enable explicit decomposition, allowing their results to be directly used in graphics engines like Maya or Blender (Autodesk, INC.; Community, 2018). However, mesh optimization is typically more challenging than implicit fields, which often struggle with complex geometry (*e.g.*, thin structures), and is generally limited to object-level reconstructions. Recently, 3D Gaussian Splatting (3DGS) (Kerbl et al., 2023a) has emerged as a powerful representation for novel view synthesis. However, its geometry is often misaligned with the ground truth surface and prone to floaters. To improve this, SuGaR (Guédon & Lepetit, 2024) introduced a set of regularizations to ensure Gaussian points closely adhere to the surface. 2DGS (Huang et al., 2024) squeezed 3D Gaussian ellipsoids into 2D Gaussian surfaces and applied dist loss (Barron et al., 2022) to improve surface accuracy. GSDF (Yu et al., 2024) and GaussianRooms (Xiang et al., 2024) jointly trained 3DGS with implicit SDF fields to supervise each other. However, these approaches keep 3DGS and SDF separate, which may lead to local minima. In contrast, we combine explicit mesh representation and 3DGS in a unified framework, training the networks in an end-to-end fashion and enabling material and lighting decomposition.

Inverse Rendering with Gaussian Splatting While the vanilla 3DGS is not designed for inverse rendering tasks, a branch of research extends it for estimating materials and lighting (Gao et al., 2023; Jiang et al., 2023; Shi et al., 2023). The key challenge lies in accurately modeling local geometry to obtain precise normal in the rendering equations. Different methods have employed various strategies to address this issue. For instance, R3DG (Gao et al., 2023) learns additional normal attributes and regularizes normal directions using rendered depth maps. GS-Shader (Jiang et al., 2023) utilizes the shortest axis direction, while GIR (Shi et al., 2023) employs eigen decomposition to determine surface orientations. These methods also incorporate the Disney BRDF (McAuley et al., 2012; Burley, 2012) with split-sum simplification (Karis, 2013) and consider indirect lighting through ray tracing or residual terms. In contrast, our approach bridges isosurface and Gaussian together, which naturally results in more accurate local geometry and normal directions, therefore bringing better inverse rendering performance.

3 Methodology

We now present a detailed description of our method. In Sec. 3.1, we introduce geometry-guided Gaussian Splatting, where the Gaussian points are generated on the isosurface. Next, in Sec. 3.2, we extend the standard Gaussian rendering equations by incorporating physically-based rendering (PBR) to account for higher-order lighting effects. Finally, in Sec. 3.3, we discuss the training strategies, loss functions, and other key implementation details.

3.1 GEOMETRY GUIDED GAUSSIAN POINTS GENERATION

Background In the vanilla 3DGS (Kerbl et al., 2023b) paper, a Gaussian ellipsoid is represented by a full 3D covariance matrix $\mathbf{\Sigma}$ and its center position $\boldsymbol{\mu}$: $G(\mathbf{x}) = e^{-\frac{1}{2}(\mathbf{x}-\boldsymbol{\mu})^T\mathbf{\Sigma}^{-1}(\mathbf{x}-\boldsymbol{\mu})}$, where $\mathbf{x}$ is the location of a 3D point. To ensure a valid positive semi-definite covariance matrix, $\mathbf{\Sigma}$ is decomposed into the scaling matrix $\mathbf{S}$ and the rotation matrix $\mathbf{R}$ that characterizes the geometry of a 3D Gaussian. Beyond $\boldsymbol{\mu}$, $\mathbf{S}$ and $\mathbf{R}$, each Gaussian maintains additional learnable parameters including opacity $o \in (0, 1)$ and Spherical Harmonic (SH) coefficients in $\mathbb{R}^k$ representing view-dependent colors (k is related to SH order). During optimization, 3DGS adaptively controls the Gaussian distribution by splitting and cloning Gaussians in regions with large view-space positional gradients, as well as the culling of Gaussians that are nearly transparent. However, each Gaussian point is independent of others and lacks global geometry constraints, which often leads inaccurate surfaces and floaters.

Method Our goal is to introduce explicit geometric guidance to 3D Gaussian Splatting. To this end, we propose GeoSplatting, which leverages isosurface techniques (Shen et al., 2021; 2023) to constrain Gaussian points to the mesh surface. Specifically, we hope to optimize a scalar function $\zeta : \mathbb{R}^3 \rightarrow \mathbb{R}$, which may be discretized directly as values at grid vertices or evaluated from an underlying neural network, *etc*. We employ FlexiCubes (Shen et al., 2023) as the underlying geometric representation, allowing for the extraction of an intermediate triangle mesh $\mathbf{M}$ from ζ in a differentiable manner.

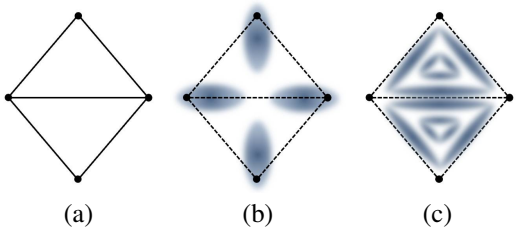

Figure 3: **MGadapter Overview**. Given surface triangles (a), we initially place one Gaussian point at each vertex (b), then densely draw six Gaussian points on each face (c).

With the intermediate mesh $\mathbf{M}$ as the explicit guidance, we then propose **MGadapter** $\mathcal{T}$ that samples Gaussian points from surface triangles in a differentiable manner to provide a bridge between mesh and Gaussian points. Specifically, the MGadapter $\mathcal{T}$ constrains the opacity and shape of the Gaussian points to ensure their alignment with the mesh $\mathbf{M}$.

We first determine the location of 3D Gaussian points from the isosurface mesh $\mathbf{M}$. As illustrated in Fig. 3, we explored various strategies and finally chose an adaptive way. At the start of the optimization, since the scalar function ζ is randomly initialized and the initial mesh contains numerous small faces, we only assign one Gaussian point to each vertex to reduce memory usage and accelerate training. As the shape gradually converges, we switch to a face-based strategy, where we empirically place six Gaussian points on each triangle face in order to capture high-frequency geometric and texture details.

The opacity for each Gaussian point is set to one, and the position $\boldsymbol{\mu}$, scale $\mathbf{S}$, and rotation $\mathbf{R}$, along with the normal $\mathbf{n}$, are determined by the local geometry (vertices or faces):

$$(\boldsymbol{\mu}, \mathbf{S}, \mathbf{R}, \mathbf{n}) = \mathcal{T}(\mathbf{M}). \tag{1}$$

Specifically, the position $\boldsymbol{\mu}$ is a barycentric interpolation of mesh vertices, the normal $\mathbf{n}$ equals the normal of corresponding mesh faces, the scale $\mathbf{S}$ and the $\mathbf{R}$ are heuristic functions relative to $\boldsymbol{\mu}$, which ensure that the shortest axis of the Gaussian point aligns with n and maintain a size that adequately covers the triangle.

Additionally, since the boundaries of Gaussian ellipsoids extend beyond their center points $\boldsymbol{\mu}$, we allow $\boldsymbol{\mu}$ to move slightly along the normal direction $\mathbf{n}$ to better align with the surface. This surface adjustment v, which is crucial for novel view synthesis, can be automatically learned via hash grids (Müller et al., 2022). Further details of MGadapter can be found in Appendix B.

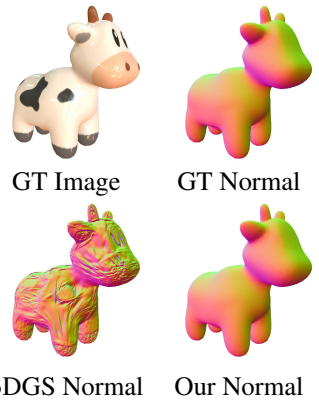

Figure 4: **Geometry-guided Normal Estimation**.

Discussion The geometry-guided MGadapter offers significant advantages over both 3DGS (Kerbl et al., 2023a) and mesh-based representations (Munkberg et al., 2022) . First, compared to 3DGS,

the geometry guidance from the isosurface provides more accurate geometry and precise surface normals without any depth or normal regularization terms, as shown in Fig. 4. This, in turn, significantly enhances the performance of inverse rendering tasks compared to prior works that rely on approximated normals. Moreover, transitioning from a mesh representation to Gaussian Splatting, *i.e.*, apply Gaussain-based rendering rather than mesh-based rendering, allows us to leverage the efficiency and representational capacity of Gaussian Splatting, enabling GeoSplatting to achieve much faster optimization time and superior novel view synthesis performance compared to NVdiffrec (Munkberg et al., 2022) as shown in our experiments.

3.2 PHYSICALLY-BASED GAUSSIAN RENDERING

The vanilla 3DGS assigns each Gaussian point a k-order spherical harmonic parameter to represent basic color and view-dependent rendering effects. In our GeoSplatting, we hope to represent high-order lighting effects with PBR materials.

Background We utilize the physically-based rendering equation (Kajiya, 1986) and GGX microfacet model (Walter et al., 2007) as follows:

$$L_{\mathrm{o}}(\boldsymbol{\omega}_{\mathrm{o}}) = \int_{\mathcal{H}^2} f_{\mathrm{r}}(\boldsymbol{\omega}_{\mathrm{i}}, \boldsymbol{\omega}_{\mathrm{o}}) L_{\mathrm{i}}(\boldsymbol{\omega}_{\mathrm{i}}) |\mathbf{n} \cdot \boldsymbol{\omega}_{\mathrm{i}}|, \mathrm{d}\boldsymbol{\omega}_{\mathrm{i}} \tag{2}$$

$$f_{\mathrm{r}}(\boldsymbol{\omega}_{\mathrm{i}}, \boldsymbol{\omega}_{\mathrm{o}}) = \frac{\mathbf{a}}{\pi} + \frac{D(\boldsymbol{\omega}_{\mathrm{i}}, \boldsymbol{\omega}_{\mathrm{o}}) F(\boldsymbol{\omega}_{\mathrm{i}}, \boldsymbol{\omega}_{\mathrm{o}}) G(\boldsymbol{\omega}_{\mathrm{i}}, \boldsymbol{\omega}_{\mathrm{o}})}{4|\mathbf{n} \cdot \boldsymbol{\omega}_{\mathrm{i}}||\mathbf{n} \cdot \boldsymbol{\omega}_{\mathrm{o}}|} \tag{3}$$

In Eq. 2, the outgoing radiance $L_{\mathrm{o}}(\boldsymbol{\omega}_{\mathrm{o}})$ in the direction $\boldsymbol{\omega}_{\mathrm{o}}$ is computed as the integral of the BRDF function $f_{\mathrm{r}}(\boldsymbol{\omega}_{\mathrm{i}}, \boldsymbol{\omega}_{\mathrm{o}})$, the incoming light $L_{\mathrm{i}}(\boldsymbol{\omega}_{\mathrm{i}})$, and the cosine term $|\mathbf{n} \cdot \boldsymbol{\omega}_{\mathrm{i}}|$, which accounts for the angle between the surface normal $\mathbf{n}$ and the incoming light direction $\boldsymbol{\omega}_{\mathrm{i}}$, over the hemisphere $\mathcal{H}^2$. In Eq. 3, the GGX model defines the BRDF function $f_{\mathrm{r}}(\boldsymbol{\omega}_{\mathrm{i}}, \boldsymbol{\omega}_{\mathrm{o}})$ as two components: the diffuse term $\frac{\mathbf{a}}{\pi}$ and the specular term $\frac{D(\boldsymbol{\omega}_{\mathrm{i}}, \boldsymbol{\omega}_{\mathrm{o}}) F(\boldsymbol{\omega}_{\mathrm{i}}, \boldsymbol{\omega}_{\mathrm{o}}) G(\boldsymbol{\omega}_{\mathrm{i}}, \boldsymbol{\omega}_{\mathrm{o}})}{4|\mathbf{n} \cdot \boldsymbol{\omega}_{\mathrm{i}}||\mathbf{n} \cdot \boldsymbol{\omega}_{\mathrm{o}}|}$. The specular term models view-dependent specular surface reflection using the normal distribution function (NDF) D, the Fresnel term F, and the geometric attenuation G. To evaluate Eq. 2 efficiently, approximation methods such as split-sum (Karis, 2013) or spherical Gaussian (Chen et al., 2021) are often used to bypass the need for the extensive Monte Carlo sampling process. Following prior works (Munkberg et al., 2022; Shi et al., 2023), we use a split-sum model:

$$L_{\mathrm{o}}(\boldsymbol{\omega}_{\mathrm{o}}) \approx \int_{\mathcal{H}^2} f_{\mathrm{r}}(\boldsymbol{\omega}_{\mathrm{i}}, \boldsymbol{\omega}_{\mathrm{o}}) |\mathbf{n} \cdot \boldsymbol{\omega}_{\mathrm{i}}| \, \mathrm{d}\boldsymbol{\omega}_{\mathrm{i}} \int_{\mathcal{H}^2} L_{\mathrm{i}}(\boldsymbol{\omega}_{\mathrm{i}}) D(\boldsymbol{\omega}_{\mathrm{i}}, \boldsymbol{\omega}_{\mathrm{o}}) |\mathbf{n} \cdot \boldsymbol{\omega}_{\mathrm{i}}| \, \mathrm{d}\boldsymbol{\omega}_{\mathrm{i}} \tag{4}$$

Eq. 4 enables fast pre-computation. The left BRDF term can be stored in a 2D lookup table and queried using $|\mathbf{n} \cdot \boldsymbol{\omega}_{\mathrm{i}}|$ and r, while the right term is represented by pre-integrated environment maps and can also be queried by r. This allows directly computing outgoing radiance L_{o} by the material parameters without any ray sampling, significantly improving rendering speed. For more details of PBR materials, please refer to (Karis, 2013; Munkberg et al., 2022).

Method Our goal is to add PBR materials to Gaussian points to produce high-order rendering effects, while still leveraging the efficient Gaussian rasterization pipeline. To achieve this, we compute the color of each Gaussian point using PBR equations, followed by Gaussian rasterization that renders the final image through alpha compositing.

Specifically, we assign each Gaussian point three PBR material parameters: a diffuse color $k_d = \frac{\mathbf{a}}{\pi} \in \mathbf{R}^3$, a roughness scalar r, and a metallic factor m. The roughness r determines the GGX normal distribution function (NDF) D, while the metallic factor m controls the specular highlight color k_s by interpolating between plastic and metallic appearances: $k_s = (1 - m) \times 0.04 + m \times k_d$. Finally, the color c_i of the i-th Gaussian point is computed as:

$$c_i = c_i^d + c_i^s + c_i^r \tag{5}$$

where c_i^d and c_i^s represent the diffuse and specular components computed using the split-sum model. In addition, we learn a residual color c_i^r (Jiang et al., 2023) to account for high-order indirect lighting effects. Once the color computation is complete, we apply the efficient Gaussian rasterization pipeline to render the points into an RGB image I and an alpha map M:

$$I = \sum_{i=1}^{N} c_i \alpha_i \prod_{j=1}^{i-1} (1 - \alpha_j), \quad M = \sum_{i=1}^{N} \alpha_i \prod_{j=1}^{i-1} (1 - \alpha_j) \tag{6}$$

where α is the projected opacity of each Gaussian. During rendering, we cull Gaussian points on back faces by checking the angle between surface normals and view directions.

Reference PBR Rendering Diffuse c^d Specular c^s Residual c^r ($\times 2.5$)

Figure 5: **PBR Rendering Decomposition**. Our PBR framework successfully disentangles the materials and lighting, capturing meaningful diffuse, specular and residual terms (Eq. 5). Note the residual image even learns the inter-reflection effects (the most shiny ball reflects a small green ball).

Discussion Our PBR pipeline enables both high-order PBR effects and efficient rendering speed. First, the PBR model allows us to capture specular, view-dependent lighting effects. Additionally, the residual component helps model inter-reflection effects beyond the capabilities of the split-sum model. Moreover, since the color is computed at each Gaussian point, the fast Gaussian rasterization pipeline can be directly employed to generate the final images. Fig. 5 shows examples of the decomposition of each lighting component of our methods.

3.3 Implementation Details

Modeling PBR Attributes GeoSplatting constrains the shape and opacity of each Gaussian point based on the corresponding surface triangle, and learns the PBR material attributes by querying MLP (Müller et al., 2022). Specifically, for the geometry, we optimize a 96^3 grid using FlexiCubes (Shen et al., 2023). For each Gaussian point, we query its corresponding surface movement v, diffuse color k_d, roughness r, specular k_s and residual color c^r from a spatial MLP (Müller et al., 2022) F: $(v, k_d, r, m, c^r) = F(\boldsymbol{\mu})$. Additionally, we learn a $6 \times 512 \times 512 \times 3$ environment map to model the lighting. Details of the network architecture are provided in Appendix B.5.

Loss Functions GeoSplatting is a fully differentiable pipeline that can be trained end-to-end. Thanks to the geometry guidance, we do not require any surface or normal regularization terms, such as dist loss (Barron et al., 2022) or pseudo depth normal loss (Jiang et al., 2023; Gao et al., 2023), and the network can be supervised by photometric loss. However, similar to NVdiffrec, GeoSplatting also relies on an object mask loss, as optimizing the surface is more challenging. Specifically, the photometric loss is computed as: $\mathcal{L}_{photo} = \mathcal{L}_1 + \lambda_{ssim}\mathcal{L}_{SSIM} + \lambda_{mask}\mathcal{L}_{mask}$, where $\mathcal{L}_{mask} = \mathcal{L}_2(M_{pred}, M_{gt})$. Here we set $\lambda_{ssim} = 0.2$ and $\lambda_{mask} = 5.0$. Furthermore, we add an entropy loss to constrain the shape, following DMTet and FlexiCubes (Shen et al., 2021; 2023). To achieve better decomposition, we apply light regularization and smoothness regularization on k_d and k_s, following NVdiffrec and R3DG (Munkberg et al., 2022; Gao et al., 2023). The final loss $\mathcal{L}$ is a combination of the photometric loss and the regularization losses: $\mathcal{L} = \mathcal{L}_{photo} + \lambda_{entropy}\mathcal{L}_{entropy} + \lambda_{smooth}\mathcal{L}_{smooth} + \lambda_{light}\mathcal{L}_{light}$. Details are provided in Appendix. C.

Second Stage Optimization GeoSplatting optimizes the underlying SDF while producing Gaussian points for image rendering. However, due to grid resolution limitations, we find that mesh-produced Gaussian points still struggle to capture detailed textures and thin geometric structures. To address this, we introduce a second-stage optimization where the Gaussian points are freely optimized without being constrained by the mesh. In the first stage, the mesh-generated Gaussian points already provide a refined shape and materials. Building on this, the second-stage optimization further enhances geometry and texture details, achieving significant improvements in novel view synthesis and relighting.

4 Experiments

We perform extensive experiments to verify the effectiveness of our inverse rendering method. We first evaluate novel view synthesis (NVS) in Sec. 4.1, demonstrating our superior performance over all relightable baselines. Next, we present material decomposition and relighting results of Synthetic4Relight in Sec. 4.2, showcasing our effectiveness in inverse rendering tasks. Additionally, we report geometric reconstruction accuracy in Sec. 4.3, and ablation studies in Sec. 4.5. Further implementation details can be found in the appendix. Our method is highly efficient, completing training within 15-20 minutes for the first stage and 5 minutes for the second stage—on a NVIDIA GTX 4090. The baselines are also evaluated on a single 4090, except R3DG and TensoIR on a single A100 for the CUDA OOM issue.

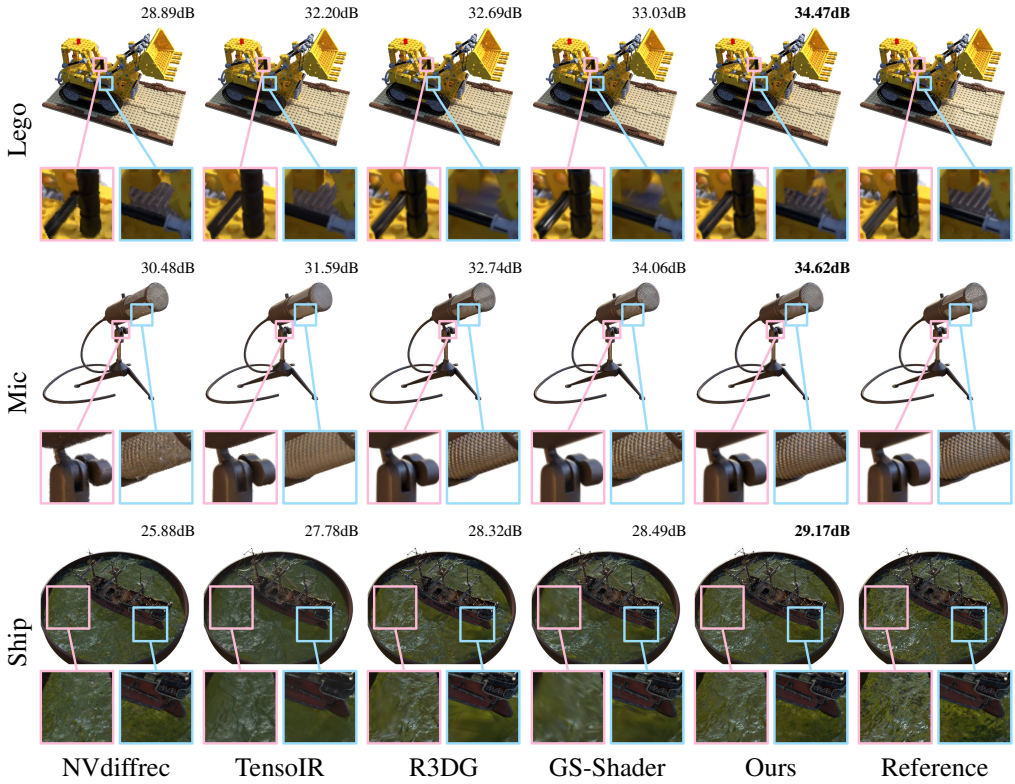

Figure 6: **Qualitative comparison on NeRF dataset**. Our method effectively recovers complex geometries, detailed textures, and non-Lambertian appearances, as shown in the sub-windows.

4.1 Performance on Novel View Synthesis

Datasets & Metrics. We evaluate NVS performance on the NeRF Synthetic dataset, which includes 8 challenging scenes featuring complex geometry and non-Lambertian materials. Following previous work, we train on 100 input views and evaluate on 200 test views. We assess NVS quality using PSNR, SSIM, and LPIPS metrics, along with training and inference times, as shown in Tbl. 1. Qualitative results are provided in Fig. 6.

Performance & Discussion. We compare our method with both non-relightable and relightable approaches. Our results achieve new state-of-the-art performance over all relightable techniques as shown in Tbl. 1. We outperform the second best method almost 1db in PSNR, demonstrating the effectiveness of our method. Compared to mesh-based representation (Munkberg et al., 2022), our method leverages the representation capability from 3DGS and achieves 3.53 PNSR improvement. Moreover, it also achieve best optimization efficiency, where each scene takes only 20 minutes. Fig. 6 shows the qualitative NVS results, where details are highlighted in the sub-windows. Compared to the baselines, our method recovers more detailed geometry (Mic) and better non-Lambertian appearance (Ship). For more results on the NeRF Synthetic dataset, please refer to Appendix H.1.

Method	Relit	PSNR↑	SSIM↑	LPIPS↓	Time↓
NeRF*	✗	31.01	0.947	0.081	1380
MipNeRF*	✗	33.09	0.961	0.043	2880
3DGS	✗	**33.17**	**0.988**	0.029	**5.4**
2DGS	✗	33.07	0.967	**0.025**	10.2
TensoIR	✓	29.53	0.944	0.050	270
NVdiffrec	✓	28.79	0.937	0.056	72
GS-IR	✓	28.57	0.922	0.076	21.6
R3DG	✓	30.15	0.954	0.044	141
GS-Shader	✓	31.45	0.959	0.034	63
Ours	✓	**32.32**	**0.962**	**0.027**	**20**

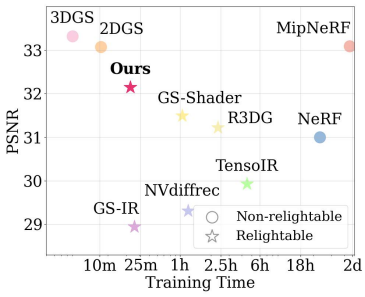

Table 1: **Quantatitive comparison on NeRF dataset** (* means copied from original papers). In the left table, ours results outperform all the relightable baseline methods in terms of both rendering quality and training efficiency (measured by average training minutes). In the right figure, we provide an intuitive overview, with the top-left corner representing superior performance. Notably, our method achieves the best results among all relightable approaches (indicated by a star marker).

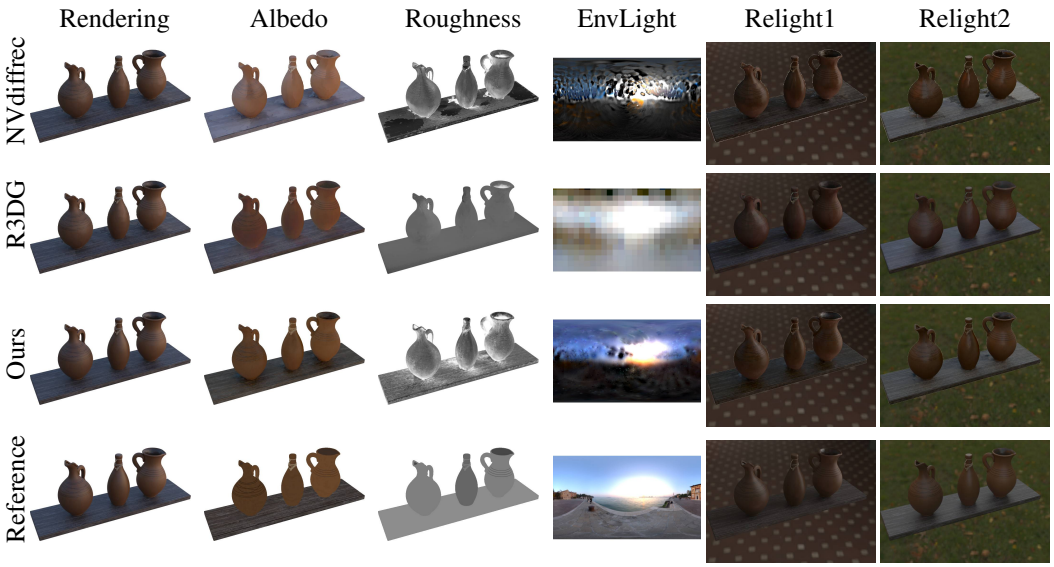

Figure 7: **Qualitative comparison of material decomposition & relighting on Synthetic4Relight Dataset**. Our method successfully recovers accurate albedo and lighting, though the roughness is slightly affected by indirect inter-reflections. Nevertheless, it still achieves the best relighting effects.

4.2 Performance on Object decomposition & Relighting

Datasets & Metrics. We evaluate Material decomposition and relighting performance on the Synthetic4Relight dataset (Zhang et al., 2022), which includes 4 challenging scenes with complex non-Lambertian materials and indirect lighting effects. Following (Gao et al., 2023), we assess NVS, Relighting, Albedo quality using PSNR, SSIM, and LPIPS metrics, along with Roughness MSE, as shown in Tbl. 2. Qualitative results are provided in Fig. 7.

Performance & Discussion. We compare our method with mesh-based (NVdiffrec) and Gaussian-based relightable approaches (R3DG, GS-Shader, GS-IR). As shown in Tbl. 2 and Fig. 7, while our method significantly outperforms the baseline methods in novel view synthesis, we also achieve state-of-the-art performance in relighting and albedo assessment, demonstrating superior material and lighting disentanglement. In terms of roughness estimation, our method performs on par with R3DG. In scenarios involving self-occlusion, our approach tends to integrate shadow effects into albedo or roughness. This behavior arises primarily from the limitations of the split-sum approximation used in our method. A detailed explanation is provided in Appendix D. To further clarify these observations, we include additional qualitative examples in Appendix H.2. Experimental results from the Shiny Blender dataset (Verbin et al., 2022b) and the TensoIR Synthetic dataset (Jin et al., 2023) are also presented in Appendices H.3 and H.4, respectively, to reinforce our findings and offer broader context.

Method	Novel View Synthesis			Relighting			Albedo			Roughness
	PSNR ↑	SSIM ↑	LPIPS ↓	PSNR ↑	SSIM ↑	LPIPS ↓	PSNR ↑	SSIM ↑	LPIPS ↓	MSE ↓
NVdiffrec	34.99	0.979	0.034	28.89	0.953	0.061	<u>28.66</u>	0.941	0.066	0.026
GS-IR	33.85	0.964	0.050	23.81	0.902	0.086	26.66	0.936	0.085	0.825
GS-Shader	30.26	0.974	0.029	22.32	0.924	0.084	N/A	N/A	N/A	0.050
R3DG*	<u>36.80</u>	<u>0.982</u>	<u>0.028</u>	<u>31.00</u>	0.964	<u>0.050</u>	28.31	<u>0.951</u>	**0.058**	**0.013**
Ours	**39.20**	**0.988**	**0.013**	**31.65**	**0.971**	**0.032**	**29.21**	**0.952**	<u>0.062</u>	<u>0.017</u>

Table 2: **Quantitative Results on the Synthetic4Relight Dataset** (* means copied from original papers). Our method achieves the best performance in NVS, relighting, and albedo, and on-par performance in roughness compared to R3DG. Note that GS-Shader does not provide disentangled albedo but rather a diffuse color merged with lighting, so we leave it as N/A. Also, note that we apply the albedo scaling introduced in (Zhang et al., 2021b) to perform a fair comparison.

4.3 Performance on Geometry recovery

Datasets & Metrics. We evaluate geometry recovery performance on four deliberately selected scenes: Spot, Damicornis, Lego, and Chair, each chosen for its distinct characteristics. Spot is

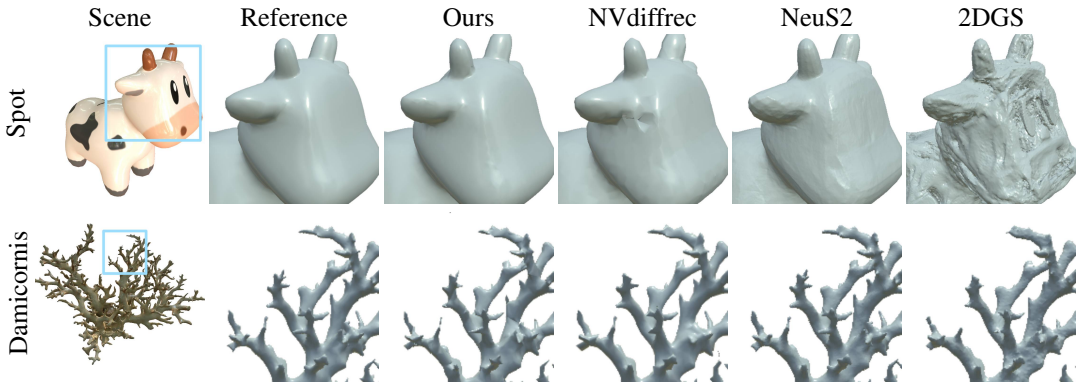

Figure 8: **Qualitative Geometry Comparison**. Our method achieves accurate geometry in scenes with challenging lighting and material conditions (shiny Spot) and complex topology (Damicornis).

highly reflective, Damicornis and Lego feature complex geometries, and Chair contains detailed textures. Following (Munkberg et al., 2022), we assess performance using the Chamfer distance and F-score, as shown in Tbl. 3. Since our method includes meshes in stage 1 and Gaussian points in both stages 1 and 2, we provide metrics for each. Qualitative results are shown in Fig. 8.

Performance & Discussion. We compare our method with SDF-based (NeuS2), mesh-based (NVdiffrec), and Gaussian-based (2DGS) approaches. As demonstrated in Table 3 and Figure 8, our method shows robust performance across diverse scenarios. In highly reflective cases (Spot), NeuS2 and 2DGS struggle to accurately capture geometry due to their limited inverse rendering capabilities. For other scenes with more intricate geometry, our approach still achieves comparable geometry recovery performance to state-of-the-art surface reconstruction techniques, underscoring the effectiveness of our intermediate mesh guidance strategy. In Appendix H.3, we present a normal quality comparison on the Shiny Blender dataset (Verbin et al., 2022b) with challenging reflective scenarios, further highlighting how our geometry guidance enhances performance in inverse rendering tasks.

Method	Spot		Damicornis		Lego		Chair	
	Chamfer ↓	F-score ↑	Chamfer ↓	F-score ↑	Chamfer ↓	F-score ↑	Chamfer ↓	F-score ↑
NeuS2	12.43	0.9773	**0.12**	0.9986	**7.03**	**0.9187**	7.94	0.9046
2DGS	39.13	0.6588	0.40	**0.9993**	13.23	0.9169	3.56	**0.9594**
NVdiffrec	1.04	0.9921	0.27	0.9974	11.38	0.8506	5.76	0.9359
Ours (Stage1 Points)	0.53	0.9995	16.56	0.9969	11.34	0.9027	4.20	0.9442
Ours (Stage2 Points)	0.49	0.9995	12.40	0.9980	8.71	0.9130	**3.11**	0.9570
Ours (Mesh)	**0.16**	**0.9997**	0.55	0.9985	9.03	0.8886	5.37	0.9254

Table 3: **Quantitative results on Geometry Recovery**. With each scene normalized to the range $[-1, 1]^3$, we report the Chamfer distance (scaled by 10^{-4}) and the F-score (under a threshold of 10^{-3}). While performing on par with other state-of-the-art methods in Lego, Chair and Damicornis, GeoSplatting achieves the best geometry in challenging reflective cases (Spot), thanks to its strong inverse rendering capabilities.

4.4 Performance on Real-world Dataset

Datasets, Performance & Discussion. Lastly, we show qualitative results on real-world DTU dataset (Aanæs et al., 2016). While GeoSplatting successfully decomposes reasonable geometry and material, as shown in Fig. 9, the real-world data is still much more challenging than synthetic data due to the inaccurate camera, complex lighting, and self occlusions. For instance, an overestimated roughness can be observed in Scan 65, mainly due to overexposure of input views. More failure cases on DTU dataset are provided in Appendix G.

4.5 Ablation Studies.

Second Stage Optimization. The second stage optimization plays a crucial role in improving the performance of novel view synthesis. On the NeRF Synthetic Dataset, it helps improve the PSNR from 29.52 to 32.32 (see Tbl. 8 in Appendix H.1). The key issue lies in the isosurface's reliance on grid sampling (96^3 for FlexiCubes), which struggles to represent detailed geometry and textures. Therefore, in the second stage, we optimize the Gaussian representation without the constraints of

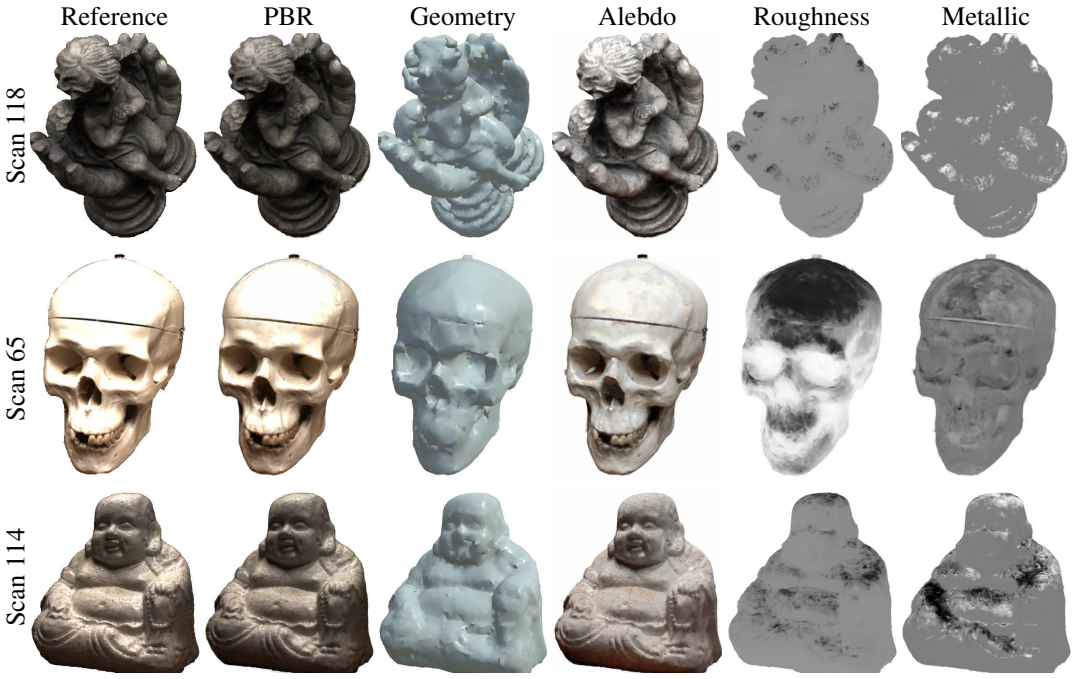

Figure 9: **Qualitative Results on DTU dataset**. Our method successfully recovers meaningful geometry and material on the challenging real-world dataset.

the mesh, allowing it to fully express its representational power. Moreover, the good initialization in the first stage still guides the optimization toward meaningful decomposition. As shown in Fig. 10, the second stage significantly enhances the performance on normal leading to improved NVS results.

Residual Terms. We find it also helps improve the performance of novel view synthesis, *e.g.*, in the Chair scene, the PSNR drops by 2dB without residual terms. GeoSplatting applies a split-sum model to represent PBR lighting effects. While it achieves delicate decomposition results, it assumes a single-bounce rendering process, *i.e.*, light hits an object and reflects back to the light source, without considering any inter-reflection effects. The inclusion of residual terms significantly improves inverse rendering performance by attributing noise and higher-order lighting effects to the residual terms. As shown in Fig. 5, it successfully models the small inter-reflected green ball.

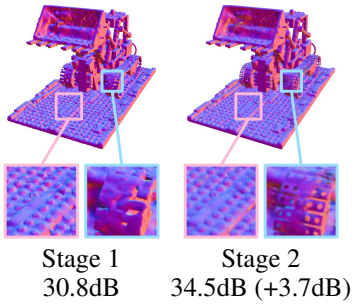

Figure 10: Second Stage Optimization on Lego.

5 Conclusion

Limitation: While GeoSplatting demonstrates state-of-the-art performance in NVS and relighting tasks, it still faces several challenges that motivate further research. First, its geometry guidance is derived from the iso-surface. Although this significantly improves the geometry performance of 3DGS, it also requires masks during training and is constrained by grid resolution, which limits its application to object-level inverse rendering tasks. A promising direction for future work would be to explore how to eliminate the need for masks and to apply adaptive resolution to accommodate detailed geometry, enabling its extension to scene-level tasks. Furthermore, GeoSplatting currently models only single-bounce specular lighting, leaving the higher-order effects (*e.g.*, inter-reflections) to residual terms. Shadows will be baked into albedo as well, resulting in an inaccurate appearance under relighting conditions. However, since we have access to intermediate meshes, incorporating ray tracing techniques could enable a more comprehensive decomposition of shadows and inter-reflections. These areas hold great potential, and we aim to explore them in future work.

Conclusion: We propose GeoSplatting, a novel hybrid representation that enhances 3DGS with explicit geometric guidance and differentiable PBR equations. GeoSplatting is highly efficient and has demonstrated state-of-the-art performance on inverse rendering tasks. We will release all the code to facilitate related research.

REFERENCES

Henrik Aanæs, Rasmus Ramsbøl Jensen, George Vogiatzis, Engin Tola, and Anders Bjorholm Dahl. Large-scale data for multiple-view stereopsis. *International Journal of Computer Vision*, 120: 153–168, 2016.

Autodesk, INC. Maya. URL https:/autodesk.com/maya.

Jonathan T Barron, Ben Mildenhall, Dor Verbin, Pratul P Srinivasan, and Peter Hedman. Mip-nerf 360: Unbounded anti-aliased neural radiance fields. In *Proceedings of the IEEE/CVF Conference on Computer Vision and Pattern Recognition*, pp. 5470–5479, 2022.

Mark Boss, Raphael Braun, Varun Jampani, Jonathan T. Barron, Ce Liu, and Hendrik P.A. Lensch. Nerd: Neural reflectance decomposition from image collections. In *IEEE International Conference on Computer Vision (ICCV)*, 2021a.

Mark Boss, Varun Jampani, Raphael Braun, Ce Liu, Jonathan T. Barron, and Hendrik P.A. Lensch. Neural-pil: Neural pre-integrated lighting for reflectance decomposition. In *Advances in Neural Information Processing Systems (NeurIPS)*, 2021b.

Brent Burley. Physically-based shading at disney. 2012. URL https://api.semanticscholar.org/CorpusID:7260137.

Wenzheng Chen, Huan Ling, Jun Gao, Edward Smith, Jaako Lehtinen, Alec Jacobson, and Sanja Fidler. Learning to predict 3d objects with an interpolation-based differentiable renderer. In *NeurIPS*, 2019.

Wenzheng Chen, Joey Litalien, Jun Gao, Zian Wang, Clement Fuji Tsang, Sameh Khalis, Or Litany, and Sanja Fidler. DIB-R++: Learning to predict lighting and material with a hybrid differentiable renderer. In *Advances in Neural Information Processing Systems (NeurIPS)*, 2021.

Blender Online Community. *Blender - a 3D modelling and rendering package*. Blender Foundation, Stichting Blender Foundation, Amsterdam, 2018. URL http://www.blender.org.

Robert A. Drebin, Loren Carpenter, and Pat Hanrahan. Volume rendering. In *Proceedings of the 15th Annual Conference on Computer Graphics and Interactive Techniques*, SIGGRAPH '88, pp. 65–74, New York, NY, USA, 1988. Association for Computing Machinery. ISBN 0897912756. doi: 10.1145/54852.378484. URL https://doi.org/10.1145/54852.378484.

Alex Fisher, Ricardo Cannizzaro, Madeleine Cochrane, Chatura Nagahawatte, and Jennifer L Palmer. Colmap: A memory-efficient occupancy grid mapping framework. *Robotics and Autonomous Systems*, 142:103755, 2021.

Jian Gao, Chun Gu, Youtian Lin, Hao Zhu, Xun Cao, Li Zhang, and Yao Yao. Relightable 3d gaussian: Real-time point cloud relighting with brdf decomposition and ray tracing. *arXiv:2311.16043*, 2023.

Wenhang Ge, Tao Hu, Haoyu Zhao, Shu Liu, and Ying-Cong Chen. Ref-neus: Ambiguity-reduced neural implicit surface learning for multi-view reconstruction with reflection. *arXiv preprint arXiv:2303.10840*, 2023.

Antoine Guédon and Vincent Lepetit. Sugar: Surface-aligned gaussian splatting for efficient 3d mesh reconstruction and high-quality mesh rendering. *CVPR*, 2024.

Jon Hasselgren, Nikolai Hofmann, and Jacob Munkberg. Shape, Light, and Material Decomposition from Images using Monte Carlo Rendering and Denoising. *arXiv:2206.03380*, 2022.

Binbin Huang, Zehao Yu, Anpei Chen, Andreas Geiger, and Shenghua Gao. 2d gaussian splatting for geometrically accurate radiance fields. In *SIGGRAPH 2024 Conference Papers*. Association for Computing Machinery, 2024. doi: 10.1145/3641519.3657428.

Yingwenqi Jiang, Jiadong Tu, Yuan Liu, Xifeng Gao, Xiaoxiao Long, Wenping Wang, and Yuexin Ma. Gaussianshader: 3d gaussian splatting with shading functions for reflective surfaces. *arXiv preprint arXiv:2311.17977*, 2023.

Haian Jin, Isabella Liu, Peijia Xu, Xiaoshuai Zhang, Songfang Han, Sai Bi, Xiaowei Zhou, Zexiang Xu, and Hao Su. Tensoir: Tensorial inverse rendering. In *Proceedings of the IEEE/CVF Conference on Computer Vision and Pattern Recognition*, pp. 165–174, 2023.

James T. Kajiya. The rendering equation. *SIGGRAPH Comput. Graph.*, 20(4):143–150, August 1986. ISSN 0097-8930. doi: 10.1145/15886.15902. URL https://doi.org/10.1145/15886.15902.

Brian Karis. Real shading in unreal engine 4. Technical report, Epic Games, 2013. URL http://blog.selfshadow.com/publications/s2013-shading-course/karis/s2013_pbs_epic_notes_v2.pdf.

Bernhard Kerbl, Georgios Kopanas, Thomas Leimkühler, and George Drettakis. 3d gaussian splatting for real-time radiance field rendering. *ACM Transactions on Graphics (ToG)*, 42(4):1–14, 2023a.

Bernhard Kerbl, Georgios Kopanas, Thomas Leimkühler, and George Drettakis. 3d gaussian splatting for real-time radiance field rendering. *ACM Transactions on Graphics*, 42(4), July 2023b. URL https://repo-sam.inria.fr/fungraph/3d-gaussian-splatting/.

Samuli Laine, Janne Hellsten, Tero Karras, Yeongho Seol, Jaakko Lehtinen, and Timo Aila. Modular primitives for high-performance differentiable rendering. *ACM Transactions on Graphics*, 39(6), 2020.

Ruofan Liang, Huiting Chen, Chunlin Li, Fan Chen, Selvakumar Panneer, and Nandita Vijaykumar. Envidr: Implicit differentiable renderer with neural environment lighting. *arXiv preprint arXiv:2303.13022*, 2023.

Stephen McAuley, Stephen Hill, Naty Hoffman, Yoshiharu Gotanda, Brian Smits, Brent Burley, and Adam Martinez. Practical physically-based shading in film and game production. In *ACM SIGGRAPH 2012 Courses*, SIGGRAPH '12, New York, NY, USA, 2012. Association for Computing Machinery. ISBN 9781450316781. doi: 10.1145/2343483.2343493. URL https://doi.org/10.1145/2343483.2343493.

B Mildenhall, PP Srinivasan, M Tancik, JT Barron, R Ramamoorthi, and R Ng. Nerf: Representing scenes as neural radiance fields for view synthesis. In *European conference on computer vision*, 2020.

Thomas Müller. tiny-cuda-nn, 4 2021. URL https://github.com/NVlabs/tiny-cuda-nn.

Thomas Müller, Alex Evans, Christoph Schied, and Alexander Keller. Instant neural graphics primitives with a multiresolution hash encoding. *ACM Transactions on Graphics (ToG)*, 41(4):1–15, 2022.

Jacob Munkberg, Jon Hasselgren, Tianchang Shen, Jun Gao, Wenzheng Chen, Alex Evans, Thomas Müller, and Sanja Fidler. Extracting Triangular 3D Models, Materials, and Lighting From Images. In *Proceedings of the IEEE/CVF Conference on Computer Vision and Pattern Recognition (CVPR)*, pp. 8280–8290, June 2022.

Johannes L Schonberger and Jan-Michael Frahm. Structure-from-motion revisited. In *Proceedings of the IEEE conference on computer vision and pattern recognition*, pp. 4104–4113, 2016.

Tianchang Shen, Jun Gao, Kangxue Yin, Ming-Yu Liu, and Sanja Fidler. Deep marching tetrahedra: a hybrid representation for high-resolution 3d shape synthesis. In *Advances in Neural Information Processing Systems (NeurIPS)*, 2021.

Tianchang Shen, Jacob Munkberg, Jon Hasselgren, Kangxue Yin, Zian Wang, Wenzheng Chen, Zan Gojcic, Sanja Fidler, Nicholas Sharp, and Jun Gao. Flexible isosurface extraction for gradient-based mesh optimization. *ACM Trans. Graph.*, 42(4), jul 2023. ISSN 0730-0301. doi: 10.1145/3592430. URL https://doi.org/10.1145/3592430.

Yahao Shi, Yanmin Wu, Chenming Wu, Xing Liu, Chen Zhao, Haocheng Feng, Jingtuo Liu, Liangjun Zhang, Jian Zhang, Bin Zhou, Errui Ding, and Jingdong Wang. Gir: 3d gaussian inverse rendering for relightable scene factorization. *Arxiv*, 2023.

Dor Verbin, Peter Hedman, Ben Mildenhall, Todd Zickler, Jonathan T Barron, and Pratul P Srinivasan. Ref-nerf: Structured view-dependent appearance for neural radiance fields. In *2022 IEEE/CVF Conference on Computer Vision and Pattern Recognition (CVPR)*, pp. 5481–5490. IEEE, 2022a.

Dor Verbin, Peter Hedman, Ben Mildenhall, Todd Zickler, Jonathan T. Barron, and Pratul P. Srinivasan. Ref-NeRF: Structured view-dependent appearance for neural radiance fields. *CVPR*, 2022b.

Bruce Walter, Stephen R. Marschner, Hongsong Li, and Kenneth E. Torrance. Microfacet models for refraction through rough surfaces. In *Proceedings of the 18th Eurographics Conference on Rendering Techniques*, EGSR'07, pp. 195–206, Goslar, DEU, 2007. Eurographics Association. ISBN 9783905673524.

Peng Wang, Lingjie Liu, Yuan Liu, Christian Theobalt, Taku Komura, and Wenping Wang. Neus: Learning neural implicit surfaces by volume rendering for multi-view reconstruction. *NeurIPS*, 2021.

Haodong Xiang, Xinghui Li, Xiansong Lai, Wanting Zhang, Zhichao Liao, Kai Cheng, and Xueping Liu. Gaussianroom: Improving 3d gaussian splatting with sdf guidance and monocular cues for indoor scene reconstruction, 2024. URL `https://arxiv.org/abs/2405.19671`.

Lior Yariv, Jiatao Gu, Yoni Kasten, and Yaron Lipman. Volume rendering of neural implicit surfaces. In *Thirty-Fifth Conference on Neural Information Processing Systems*, 2021.

Mulin Yu, Tao Lu, Linning Xu, Lihan Jiang, Yuanbo Xiangli, and Bo Dai. Gsdf: 3dgs meets sdf for improved rendering and reconstruction, 2024. URL `https://arxiv.org/abs/2403.16964`.

Kai Zhang, Fujun Luan, Qianqian Wang, Kavita Bala, and Noah Snavely. PhySG: Inverse rendering with spherical gaussians for physics-based material editing and relighting. In *The IEEE/CVF Conference on Computer Vision and Pattern Recognition (CVPR)*, 2021a.

Xiuming Zhang, Pratul P Srinivasan, Boyang Deng, Paul Debevec, William T Freeman, and Jonathan T Barron. Nerfactor: Neural factorization of shape and reflectance under an unknown illumination. *ACM Transactions on Graphics (ToG)*, 40(6):1–18, 2021b.

Yuanqing Zhang, Jiaming Sun, Xingyi He, Huan Fu, Rongfei Jia, and Xiaowei Zhou. Modeling indirect illumination for inverse rendering. In *CVPR*, 2022.

Matthias Zwicker, Jussi Rasanen, Mario Botsch, Carsten Dachsbacher, and Mark Pauly. Perspective accurate splatting. In *Proceedings-Graphics Interface*, pp. 247–254, 2004.

A APPENDIX

In the appendix, we provide a comprehensive explanation about the details of our work, including detailed implementations and limitations of our method, as well as supplementary results from both quantitative and qualitative experiments.

The appendix begins with a detailed explanation of the MGadapter in Appendix B, followed by an overview of the implementation details for our loss functions in Appendix C. In Appendix D, we analyze two approaches for PBR computation (split-sum and spherical Gaussian) before examining the impact of different FlexiCubes resolutions in Appendix E. To explore the limitations of our method, we include an ablation study on the input mask required during training in Appendix F, as well as an analysis of failure cases in Appendix G. Finally, we present additional results from novel view synthesis (NVS) and relighting experiments in Appendix H.

B EXPLANATION OF MGADAPTER

B.1 OVERVIEW

We first describe the details of our MGadapter. As discussed in Sec. 3.1, the MGadapter takes a triangle mesh as input and generates a set of Gaussian points corresponding to the mesh's shape. The core idea of MGadapter is to ensure that the shape of the triangle mesh aligns with that of the Gaussian points, serving as a differentiable adapter between the two. However, since Gaussian points lack the discrete geometric boundaries present in meshes, we define geometric alignment as follows: given a triangle face, we can sample several viewpoints and render the triangle from them. The geometric alignment is then measured by the difference between the rendered mesh and the rendered Gaussian points (e.g. L_1 loss on depth maps).

The intuitive implementation of our MGadapter involves sampling several Gaussian points on the mesh surface. These points are then optimized in terms of scale and rotation to minimize the depth map difference between the Gaussian points and the target mesh. However, this approach introduces an additional optimization step that must be re-executed each time the mesh is modified, resulting in reduced optimization efficiency and an unstable training process.

Instead of performing geometric alignment in real-time, we propose utilizing a predefined heuristic function $\mathcal{T}$ to achieve an approximate alignment. As described in Eq. 1, the MGadapter $\mathcal{T}$ takes arbitrary triangle meshes as input and outputs Gaussian point attributes, including position $\boldsymbol{\mu}$, scale $\mathbf{S}$, rotation $\mathbf{R}$, and normal $\mathbf{n}$. This process acts as a generalized adapter between the input meshes and the corresponding Gaussian points. In Appendix B.2, we provide a detailed explanation of Eq. 1. Then, we discuss the implementation of the surface adjustment in Appendix B.4, which is critical for Gaussian point rendering. Finally, we explain how to query Gaussian point attributes from a spatial MLP in Appendix B.5 and explain the warm-up stage in Appendix B.3.

B.2 EXPLANATION OF EQ. 1

Specifically, given the triangle mesh, each triangle face F_i comprises three vertices $P_i = (p_{i1}, p_{i2}, p_{i3})$ with their vertex normals $N_i = (n_{i1}, n_{i2}, n_{i3})$. We symmetrically sample 6 points on F_i with barycentric coordinates:

$$\begin{aligned} b_1 &= (u, u, 1-2u) \quad b_2 = (u, 1-2u, u) \quad b_3 = (1-2u, u, u) \\ b_4 &= (v, v, 1-2v) \quad b_5 = (v, 1-2v, v) \quad b_6 = (1-2v, v, v) \end{aligned} \tag{7}$$

And we can obtain 6 midpoints m_{jk}:

$$\begin{aligned} m_{12} &= \frac{b_1+b_2}{2} = \left(u, \frac{1-u}{2}, \frac{1-u}{2}\right) \quad m_{45} = \frac{b_4+b_5}{2} = \left(v, \frac{1-v}{2}, \frac{1-v}{2}\right) \\ m_{23} &= \frac{b_2+b_3}{2} = \left(\frac{1-u}{2}, \frac{1-u}{2}, u\right) \quad m_{56} = \frac{b_5+b_6}{2} = \left(\frac{1-v}{2}, \frac{1-v}{2}, v\right) \\ m_{31} &= \frac{b_3+b_1}{2} = \left(\frac{1-u}{2}, u, \frac{1-u}{2}\right) \quad m_{64} = \frac{b_6+b_4}{2} = \left(\frac{1-v}{2}, v, \frac{1-v}{2}\right) \end{aligned} \tag{8}$$

Given an attribute $A_i = (a_{i1}, a_{i2}, a_{i3})$ defined at the triangle vertices, we represent the barycentric interpolation as:

$$(b_1, b_2, b_3) \odot A_i = b_1 a_{i1} + b_2 a_{i2} + b_3 a_{i3} \tag{9}$$

Then, for each midpoint m_{jk} $(jk = 12, 23, 31, 45, 56, 64)$, we sample a Gaussian point as:

$$\begin{aligned}
\boldsymbol{\mu} &= m_{jk} \odot P_i & \mathbf{n} &= m_{jk} \odot N_i \\
\mathbf{S}_x &= \alpha_{jk} \| b_k \odot P_i - m_{jk} \odot P_i \|_2 & \mathbf{R}_x &= \frac{b_k \odot P_i - m_{jk} \odot P_i}{\| b_k \odot P_i - m_{jk} \odot P_i \|_2} \\
\mathbf{S}_y &= \frac{\text{Area}(F_i)}{\beta_{jk} \| b_k \odot P_i - m_{jk} \odot P_i \|_2} & \mathbf{R}_y &= \mathbf{n} \times \mathbf{R}_x \\
\mathbf{S}_z &= \delta_{jk} & \mathbf{R}_z &= \mathbf{n}
\end{aligned} \tag{10}$$

Here, Eq. 10 provide the formulation of our heuristic function $\mathcal{T}$, with $u, v, \alpha_{jk}, \beta_{jk}, \delta_{jk}$ as hyper-parameters. To achieve the generalized geometric alignment, we practically set these parameters as follows:

$$\begin{aligned}
u &= 0.07 \\
v &= 0.22 \\
\alpha_{12} = \alpha_{23} = \alpha_{31} &= 0.80 \\
\alpha_{45} = \alpha_{56} = \alpha_{64} &= 2.08 \\
\beta_{12} = \beta_{23} = \beta_{31} &= 15.0 \\
\beta_{45} = \beta_{56} = \beta_{64} &= 13.0 \\
\delta_{12} = \delta_{23} = \delta_{31} = \delta_{45} = \delta_{56} = \delta_{64} &= 4.5 \times 10^{-5}
\end{aligned} \tag{11}$$

B.3 Explanation of Warm-up Stage

Next, we explain the warm-up stage during training. As outlined in Appendix B.2, we typically sample six Gaussian points from each triangle surface. However, during the initial training stage when the underlying mesh has not yet converged, there can be an excessive number of triangle slices, as illustrated in Fig. 11. Sampling six Gaussian points per face in this scenario can result in significant memory costs and reduced training efficiency.

To address this issue, we implement a warm-up stage for MGadapter at the beginning of training (covering the first 2%). During this phase, MGadapter outputs a significantly reduced number of Gaussian points by performing vertex sampling. Specifically, MGadapter samples a single Gaussian point from each mesh vertex and assigns its normal to match the corresponding vertex normal. For the scales and rotations of the sampled Gaussian points, we utilize two small spatial MLPs to learn these attributes. Once the warm-up stage concludes, the two spatial MLPs are discarded, and the scales and rotations are afterwards computed as described in Appendix B.2.

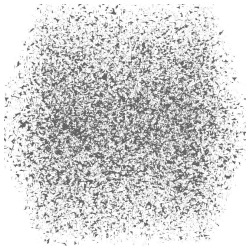

Figure 11: Initial mesh slices of FlexiCubes.

B.4 Explanation of Surface Adjustment

By applying Eq. 10, we obtain a set of Gaussian points that lie exactly on the surface. However, as mentioned in Sec. 3.1, strictly positioning the Gaussian points on the surface can negatively impact rendering quality, particularly near the boundaries between distinct texture colors.

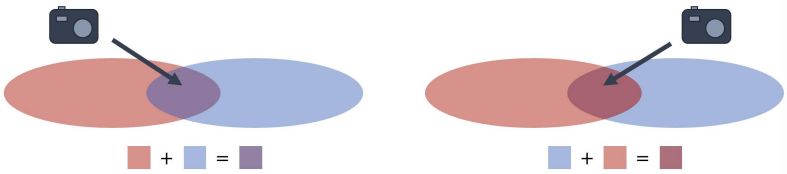

Figure 12: **Inconsistent Sorting.** The vanilla 3D splatting algorithm produces multi-view-inconsistent depths, leading to varying blending sequences across different views.

This issue primarily arises from the approximations made during the projection transformation of 3DGS, as noted in (Zwicker et al., 2004). These approximations lead to multi-view-inconsistent sorting in the overlapping regions between two surface-aligned Gaussian points, as illustrated in Fig. 12. Consequently, Gaussian points near color boundaries struggle to learn a consistent appearance. Fig. 13(a) presents rendering results when Gaussian points are strictly positioned on the surface, further demonstrating this problem. However, upon noticing that vanilla 3DGS can achieve high rendering quality despite the projection approximations, we perform further analysis and found it automatically learns to position those boundary Gaussians deeper, placing them beneath the actual surface. This adjustment results in a consistent depth sorting. Therefore, in our MGadapter, we also allow Gaussian points to learn a small offset along the normal direction. As demonstrated in Fig. 13(b), such surface adjustment can significantly enhance rendering quality, which is important for modeling reflective surface accurately in inverse rendering tasks. The magnitude of this surface adjustment (measured by $\|v\|$) is visualized in Fig. 13(c), highlighting larger adjustments near the color boundaries.

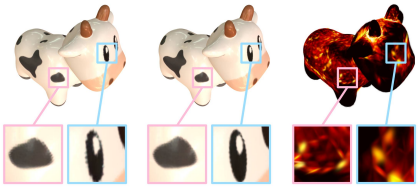

(a) w/o SA (b) w/ SA (c) Heatmap

Figure 13: **Surface Adjustment (SA) Explanation.** (a) PSNR: 31.9dB; (b) PSNR: 33.5dB; (c) Magnitude of SA.

The depth error from the projection approximation in 3DGS has also been discussed in recent work, specifically 2DGS (Huang et al., 2024). Rather than applying 3D splatting to flat Gaussian points, 2DGS employs a ray-splat intersection algorithm to ensure depth-precise rendering, resulting in a view-consistent appearance. However, when integrating the 2D splatting algorithm into our pipeline without surface adjustment, we observe strong floater artifacts, which are illustrated in Fig. 14, probably due to the incompatibility between 2DGS and FlexiCubes. Specifically, as noted in the original paper, 2D Gaussian points can degenerate into a line when observed from a slanted viewpoint. In this context, 2DGS renders these Gaussian points differently, and we empirically find it causes FlexiCubes to struggle with reducing mesh slices shown in Fig. 11, leading to unwanted floaters. We conducted a quantitative analysis comparing the two splatting algorithms, with results presented in Tbl. 4, demonstrating the incompatibility between 2DGS and FlexiCubes. Consequently, we have chosen to employ 3D splatting instead.

(a) 3D Splatting (28.43dB) (b) 2D Splatting (26.52dB)

Figure 14: **Qualitative Comparison between 2D Splatting and 3D Splatting.** Producing incorrect rendering results for tiny surfels, 2DGS encounters challenges in reducing the triangle slices initially generated by FlexiCubes, leading to noticeable floaters.

Method	Chair	Drums	Ficus	Hotdog	Lego	Materials	Mic	Ship	Avg.
Ours (3D splatting)	31.98	24.53	28.96	33.85	30.83	28.43	31.32	26.23	29.52
Ours (2D splatting)	29.44	23.71	26.34	31.18	29.86	26.52	28.21	25.22	27.56

Table 4: Splatting algorithm comparison on NeRF dataset (PSNR↑).

B.5 Explanation of Spatial MLP

Lastly, we discuss how to model PBR attributes and surface adjustments on Gaussian points. Since Gaussian points are generated in real time from the underlying mesh, directly modeling these at-

tributes as learnable parameters is impractical due to the varying number of Gaussian points during training. Instead, we employ a spatial MLP F to construct an attribute field, as mentioned in Sec. 3.3.

Specifically, the spatial MLP incorporates the multi-resolution hash encoding introduced in (Müller et al., 2022), followed by a compact MLP. For any spatial coordinate $p \in [-1, 1]^3$, the spatial MLP outputs $F(p) \in \mathbb{R}^C$. Implemented using tiny-cuda-nn (Müller, 2021), we utilize two spatial MLPs, F_{PBR} and F_{SA}, to model PBR attributes and surface adjustments, respectively. Detailed parameters can be found in Tbl. 5.

Module	Parameter	Value
$F_{\text{PBR}}/F_{\text{SA}}$ HashEnc	Number of levels	16
	Max.entries per level (hash table size)	2^{19}
	Number of feature dimensions per entry	2
	Coarsest resolution	32
	Finest resolution	4096
F_{PBR} MLP	MLP layers	$32 \times 32 \times 32 \times 6$
	Initialization	Kaiming-uniform
	Final activation	Sigmoid
F_{SA} MLP	MLP layers	$32 \times 32 \times 1$
	Initialization	Kaiming-uniform
	Final activation	None

Table 5: Parameters of Spatial MLP

C Details of Loss Functions

C.1 Photometric Term

During the training stage, for each view i, GeoSplatting differentiably renders a RGB image $I_{pred}^{(i)} \in \mathbb{R}^{H \times W \times 3}$ and takes the alpha channel as the mask $M_{pred}^{(i)} \in \mathbb{R}^{H \times W \times 1}$. Given the ground truth $I_{gt}^{(i)}$ and $M_{gt}^{(i)}$ for view i, the photometric loss is computed as:

$$\begin{aligned} \mathcal{L}_{photo} &= \mathcal{L}_1 + \lambda_{ssim}\mathcal{L}_{SSIM} + \lambda_{mask}\mathcal{L}_{mask} \\ &= \|I_{gt}^{(i)} - I_{pred}^{(i)}\|_1 + \lambda_{ssim}\text{SSIM}(I_{gt}^{(i)}, I_{pred}^{(i)}) + \lambda_{mask}\|M_{gt}^{(i)} - M_{pred}^{(i)}\|_2 \end{aligned} \tag{12}$$

Here, $\lambda_{ssim} = 0.2$ and $\lambda_{mask} = 5.0$ for all the cases.

C.2 Entropy Regularization Term

Following DMTet and FlexiCubes (Shen et al., 2021; 2023), we add an entropy loss to constrain the shape. Specifically, we employ FlexiCubes as the underlying geometric representation, which defines a scalar function $\zeta : \mathbb{R}^3 \to \mathbb{R}$ on the underlying cube grids $\mathcal{G}(\mathcal{V}, \mathcal{E})$ and then extracts isosurfaces via the differential Dual Marching Cubes introduced by (Shen et al., 2023). Given an edge (v_i, v_j) from edge set $\mathcal{E}$, the SDF values defined on the endpoints v_i, v_j are respectively $\zeta(v_i)$ and $\zeta(v_j)$.

Then, we can compute the regularization term as:

$$\mathcal{L}_{sdf} = \sum_{(v_i,v_j)\in\mathcal{E}, \text{sgn}(\zeta(v_i)) \neq \text{sgn}(\zeta(v_j))} \mathcal{H}(\zeta(v_i), \text{sgn}(\zeta(v_j))) + \mathcal{H}(\zeta(v_j), \text{sgn}(\zeta(v_i))) \tag{13}$$

Here, $\mathcal{H}$ denotes the binary cross entropy. By encouraging the same sign of ζ, such a regularization term penalize internal geometry and floaters.

C.3 Smoothness Regularization Term

Following NVdiffrec and R3DG (Munkberg et al., 2022; Gao et al., 2023), we apply smoothness regularization on albedo, roughness, and metallic to prevent dramatic high-frequency variations.

Given the positions $\boldsymbol{\mu}$ of Gaussian points, the albedo, roughness and metallic attributes are generated by the spatial MLP:

$$(v, k_d, r, m, c^r) = F(\boldsymbol{\mu}) \tag{14}$$

While applying a small perturbation on $\boldsymbol{\mu}$ can yield a different set of attributes:

$$\left(v', k_d', r', m', c^{r\prime}\right) = F(\boldsymbol{\mu} + \Delta\boldsymbol{\mu}) \tag{15}$$

The smoothness are computed as:

$$\mathcal{L}_{smooth} = \lambda_{albedo}\|k_d - k_d'\|_1 + \|r - r'\|_1 + \|m - m'\|_1 \tag{16}$$

Here, $\lambda_{albedo} = 6.0$.

C.4 Light Regularization Term

Following NVdiffrec and R3DG (Munkberg et al., 2022; Gao et al., 2023), we add white balance regularization to prevent the albedo from being baked into the environment map.

Given a learnable environment map $L \in \mathbb{R}^{6\times512\times512\times3}$ which can be split into RGB channels $L_R, L_G, L_B \in \mathbb{R}^{6\times512\times512}$, the white balance regularization is computed as:

$$\mathcal{L}_{light} = \frac{1}{3}\left(\|L_R - L_W\|_1 + \|L_G - L_W\|_1 + \|L_B - L_W\|_1\right) \tag{17}$$

where $L_W = \frac{1}{3}(L_R + L_G + L_B)$.

C.5 Final Loss

The final loss $\mathcal{L}$ is computed as:

$$\mathcal{L} = \mathcal{L}_{photo} + \lambda_{sdf}\mathcal{L}_{sdf} + \lambda_{smooth}\mathcal{L}_{smooth} + \lambda_{light}\mathcal{L}_{light} \tag{18}$$

Here, λ_{sdf} is initially set to 0.2 at the start of the training stage and is linearly decreased to 0.01 by the midpoint of the training. As for λ_{smooth} and λ_{light}, typical settings are $\lambda_{smooth} = 0.005, \lambda_{light} = 0.0005$. For highly specular objects, λ_{light} should be set to a smaller value, such as 0.00001.

D Split-Sum Approximation vs. Spherical Gaussian

The physically-based rendering (PBR) equation, incorporating the GGX microfacet model, is expressed in Eq. 2 and Eq. 3. However, solving this equation requires extensive Monte Carlo sampling, which is computationally intensive and impractical for both real-time forward rendering and inverse rendering. To address this challenge, several efficient methods for approximating the PBR equation have been proposed. The two most widely adopted approaches are the split-sum approximation (Karis, 2013) and Spherical Gaussian (SG) representations (Chen et al., 2021). While the Spherical Gaussian approximations are commonly used by inverse rendering methods such as InvRender, TensoIR, and R3DG, methods like NVdiffrec, GaussianShader, and our GeoSplatting favor the split-sum approximation due to its efficiency and ability in modeling complicated lighting.

$$L_{\mathrm{o}}(\mathbf{x}, \boldsymbol{\omega}_{\mathrm{o}}) = \int_{\mathcal{H}^2} f_{\mathrm{r}}(\mathbf{x}, \boldsymbol{\omega}_{\mathrm{i}}, \boldsymbol{\omega}_{\mathrm{o}}) L_{\mathrm{i}}(\mathbf{x}, \boldsymbol{\omega}_{\mathrm{i}}) |\mathbf{n}\cdot\boldsymbol{\omega}_{\mathrm{i}}| \mathrm{d}\boldsymbol{\omega}_{\mathrm{i}} \tag{19}$$

$$= \int_{\mathcal{H}^2} f_{\mathrm{r}}(\mathbf{x}, \boldsymbol{\omega}_{\mathrm{i}}, \boldsymbol{\omega}_{\mathrm{o}})(L_{\mathrm{ind}}(\mathbf{x}, \boldsymbol{\omega}_{\mathrm{i}}) + V(\mathbf{x}, \boldsymbol{\omega}_{\mathrm{i}}) L_{\mathrm{env}}(\boldsymbol{\omega}_{\mathrm{i}})) |\mathbf{n}\cdot\boldsymbol{\omega}_{\mathrm{i}}| \mathrm{d}\boldsymbol{\omega}_{\mathrm{i}} \tag{20}$$

To improve computational tractability, Eq. 19 can be reformulated as Eq. 20, where the incoming illumination $L_{\mathrm{i}}(\mathbf{x}, \boldsymbol{\omega}_{\mathrm{i}})$ is split into two components: the indirect lighting term $L_{\mathrm{ind}}(\mathbf{x}, \boldsymbol{\omega}_{\mathrm{i}})$ and the environment lighting term $L_{\mathrm{env}}(\boldsymbol{\omega}_{\mathrm{i}})$. This separation allows the PBR equation to be computed in two parts, the environment lighting term $L_{\mathrm{env}}(\boldsymbol{\omega}_{\mathrm{i}})$ and the light transfer terms $L_{\mathrm{ind}}(\mathbf{x}, \boldsymbol{\omega}_{\mathrm{i}})$ & $V(\mathbf{x}, \boldsymbol{\omega}_{\mathrm{i}})$, each interacting with the bidirectional reflectance distribution function (BRDF).

The split-sum approximation and Spherical Gaussian methods address different challenges in rendering complex lighting and light transfer scenarios. While both approaches have strengths, they also exhibit notable limitations.

1. The split-sum approximation excels in efficiently modeling complex environmental lighting. Its computational simplicity makes it a practical choice for scenarios where speed is critical. However, it struggles to accurately handle visibility terms. In highly occluded scenes, the errors introduced by the approximation in Eq. 4 become significant.
2. In contrast, the Spherical Gaussian approach effectively captures intricate light transfer phenomena such as inter-reflection and ambient occlusion. However, its capacity to model direct lighting is limited to low-frequency components. This restriction results in inaccuracies when dealing with highly specular surfaces, where precise decomposition is essential.

Despite the challenges posed by shadow and self-occlusion effects, as shown in Fig. 7, we choose to utilize the split-sum approximation for several compelling reasons:

1. **Efficiency in Training and Inference:** The SG-based methods integrated with ray tracing, both neural-field-based TensoIR and 3DGS-based R3DG, results in longer training times and lower inference frame rates, as highlighted in Fig. 15.
2. **Handling Reflective Cases:** SG-based methods struggle to accurately model complex lighting-material interactions in reflective scenarios, leading to subpar decomposition results, as discussed in Appendix D.1.
3. **Addressing Occlusion Challenges:** While highly occluded cases present difficulties, the inclusion of a learnable occlusion term can mitigate these issues, as detailed in Appendix D.2.

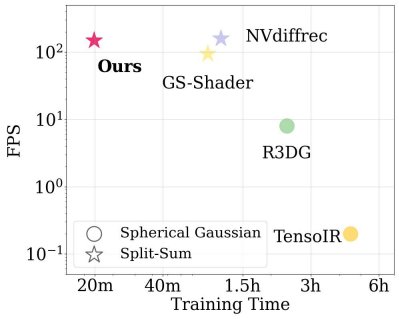

Figure 15: Comparison of Efficiency between Split-Sum and SG.

D.1 Reflective Cases

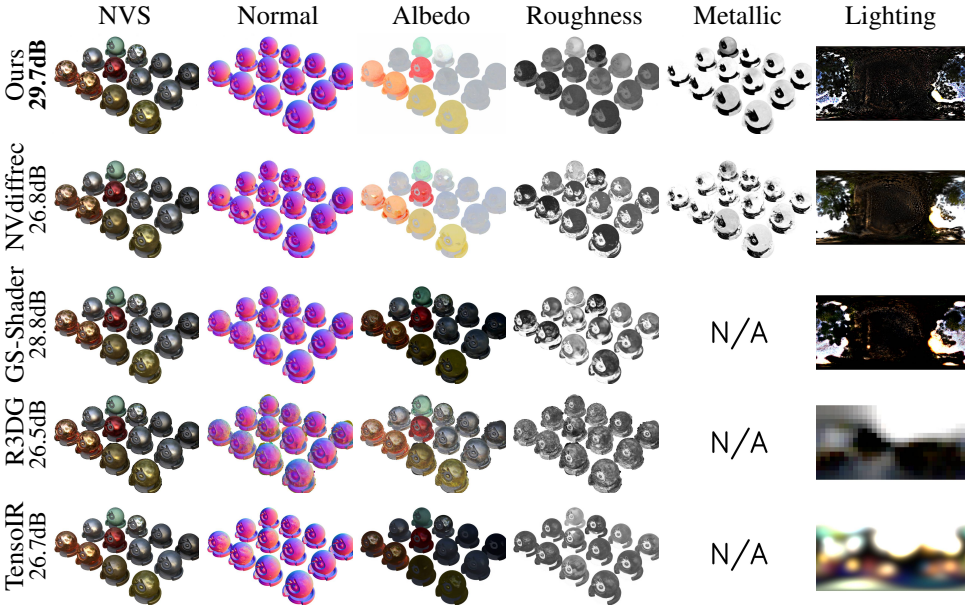

Figure 16: Incorrect Decomposition for SG-based Methods

The SG-based methods, such as TensoIR and R3DG, face significant challenges under complex lighting conditions, particularly when dealing with intricate material properties. As shown in Fig. 16, while split-sum-based methods achieve reasonable decomposition, TensoIR and R3DG fail to accurately reconstruct geometry, materials, and lighting. In Fig. 31, we provide qualitative decomposition results on the Shiny Blender dataset (Verbin et al., 2022b), to further demonstrate the strengths of our method on reflective cases.

D.2 Learnable Occlusion

Although all split-sum-based methods, including NVdiffrec and GS-Shader, struggle with self-occluded cases, it is still possible to mitigate the occlusion issue by modeling the visibility term $V(\mathbf{x}, \boldsymbol{\omega}_\mathrm{i})$ as described in Eq. 20. By introducing a learnable attribute o_i for each Gaussian point i, we reformulate Eq. 5 as follows:

$$c_i = (1 - o_i)(c_i^d + c_i^s) + c_i^r \tag{21}$$

Here, c_i^d, c_i^s and c_i^r represent diffuse, specular, and residual terms, respectively. This learnable occlusion term improves our method's ability to handle shadow effects. As shown in 17, for the Hotdog scene from the Synthetic4Relight dataset and the TensoIR Synthetic dataset, with weaker shadow effects, our occlusion term effectively aids in albedo-shadow decoupling.

Note that despite the roughness quality on the Hotdog scene remaining influenced by shadow effects, the albedo quality of our method achieves the best among the baselines, as evidenced by Table 12 in Sec. H.4. However, for the Hotdog scene from the NeRF Synthetic dataset with strong shadow effects, our method, together with other baselines, struggles with effective shadow estimation. As illustrated in Fig. 18, the results highlights shadow modeling as the long-term existing challenges in inverse rendering.

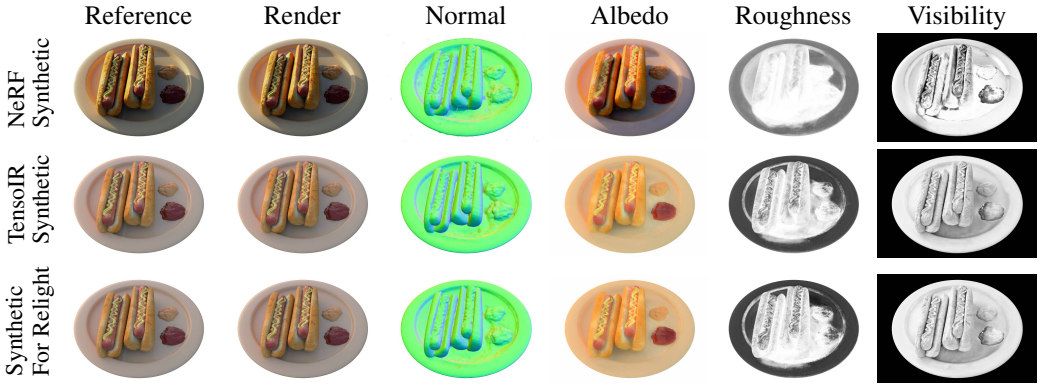

Figure 17: Qualitative comparison of decomposition performance under varying shadow effects.

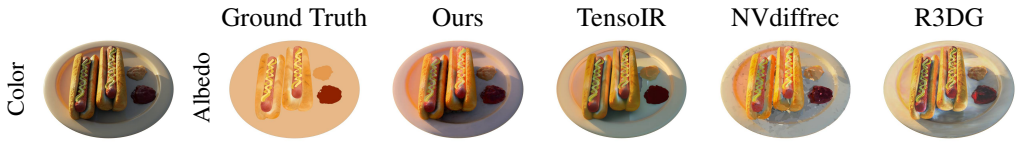

Figure 18: Qualitative results of albedo reconstruction performance under strong shadow effects.

E Analysis of FlexiCubes Resolution

In this section, we examine the impact of FlexiCubes' grid resolution on our decomposition performance, focusing on rendering quality, albedo accuracy, normal quality, and training efficiency. Quantitative results are provided in Table 6, while qualitative results are shown in Fig. 19. Although FlexiCubes with higher resolution offer more precise normal guidance, the increased computational cost and inefficient training time may not justify the benefits.

GeoSplatting Resolution	Novel View Synthesis PSNR ↑	SSIM ↑	LPIPS ↓	Albedo PSNR ↑	SSIM ↑	LPIPS ↓	Normal MAE ↓	Training Time minute(s)↓
64	36.31	0.9785	0.014	21.49	0.8799	0.128	8.451	14
96	37.15	0.9811	0.011	21.78	0.8824	0.118	7.880	24
128	37.57	0.9827	0.009	21.92	0.8825	0.117	7.313	96

Table 6: Impact of Grid Resolution on Decomposition Performance.

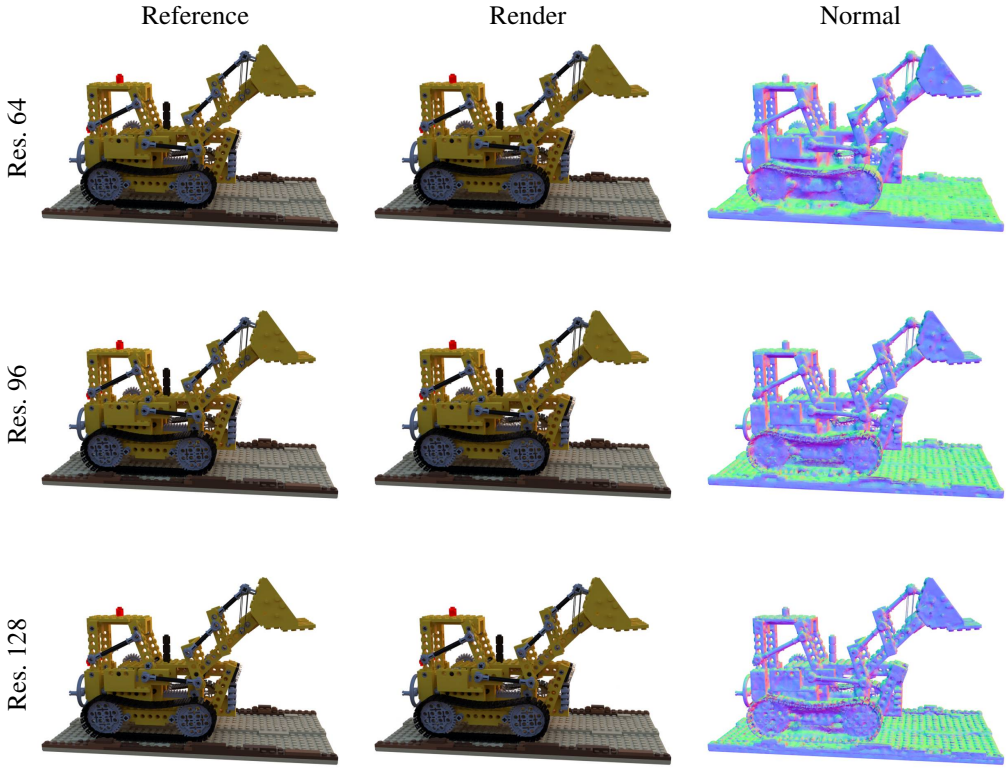

Figure 19: Qualitative Comparison of Different Grid Resolution.

F Analysis of Mask

As discussed in Appendix C.1, our method requires input masks during the training stage. Specifically, the mask term of the loss function in Eq. 12 is defined by the difference between the input masks and our predicted masks. This dependency introduces a limitation, as real-world data must first be segmented into foreground and background. To provide a comprehensive understanding, we present an ablation study to illustrate how the dependency on input masks varies across different scenes.

F.1 Object-Level

Table 7 presents the performance differences in novel view synthesis (measured in terms of PSNR) on the NeRF Synthetic Dataset, while qualitative comparison are shown in Fig. 20. The results indicate that without the mask, our method has difficulty reconstructing smooth, convex surfaces with specular highlights, as seen in Materials and Mic. Additionally, for objects with thin structures, such as Ficus, performance significantly declines in the absence of the mask loss term. In contrast, for the other five objects in the NeRF Synthetic Dataset, the ground truth mask is not essential for achieving satisfactory results.

Method	Chair	Drums	Ficus	Hotdog	Lego	Materials	Mic	Ship	Avg.
Ours w/ mask (stage 1)	31.98	24.53	28.96	33.85	30.83	28.43	31.32	26.23	29.52
Ours w/o mask (stage 1)	31.92	23.53	26.11	33.95	31.02	24.81	30.99	26.08	28.55
Difference	-0.06	-1.00	-2.85	+0.10	+0.19	-3.62	-0.33	-0.15	-0.97
Ours w/ mask (stage 2)	34.71	26.05	33.48	36.40	34.47	29.66	34.62	29.17	32.32
Ours w/o mask (stage 2)	34.81	25.72	31.56	36.36	34.73	28.22	34.31	28.54	31.78
Difference	+0.10	-0.33	-1.92	-0.04	+0.26	-1.44	-0.31	-0.63	-0.54

Table 7: Quantitative results of mask ablation study (PSNR↑).

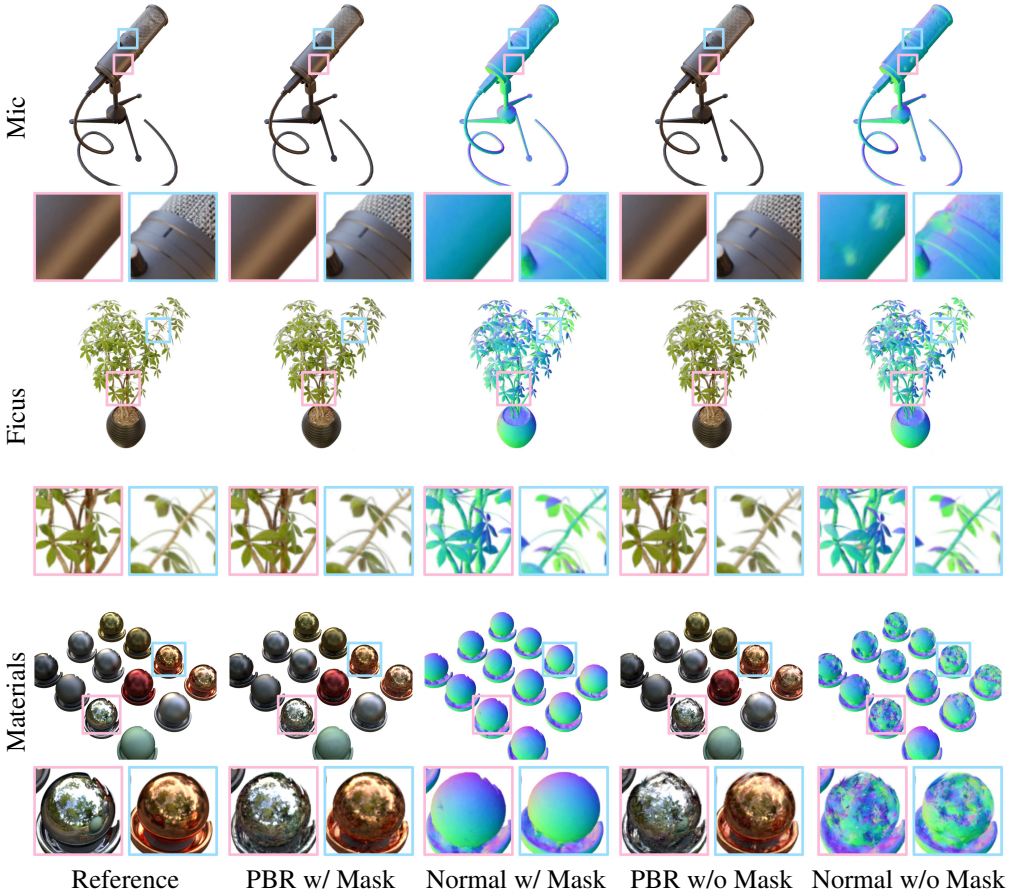

Figure 20: Qualitative results of mask ablation study.

F.2 SCENE-LEVEL

Without input masks, our method will completely fail on scene-level cases, as illustrated in Fig. 21. To extend our method from object-level decomposition to scene-level decomposition, a promising direction is to explore how to eliminate the need for masks and to apply adaptive resolution to accommodate detailed geometry.

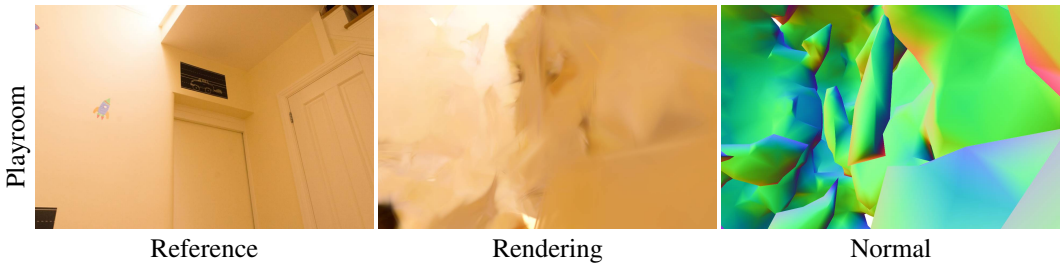

Figure 21: Failure on scene-level decomposition tasks.

G FAILURE CASES

We present a series of failure cases to illustrate the limitations of our method. The qualitative examples from both the synthetic dataset and the DTU Dataset highlight scenarios that lead to incorrect decomposition or poor geometry.

G.1 THIN STRUCTURES

As discussed in Sec. 4.5, our method struggles with thin structures in the first stage due to grid resolution limitations. While the second stage relaxes positional constraints on Gaussian points to aid in recovering fine geometry, it still cannot perfectly reconstruct thin structures due to the absence of geometric guidance in Stage 2. Fig. 22 showcases failure cases involving the Ficus, Ship, and Air Balloons.

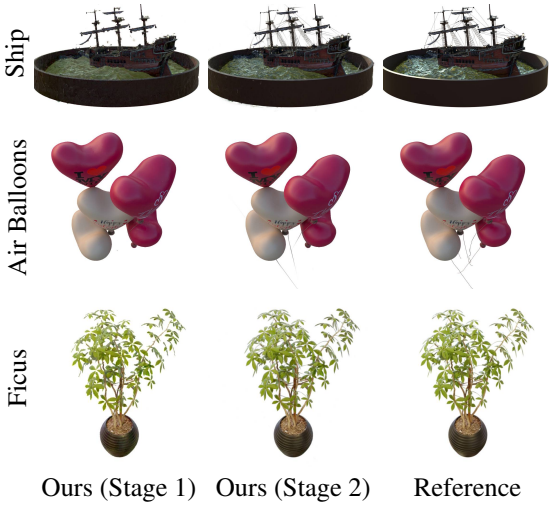

Figure 22: Failure cases of thin structures.

G.2 INCONSISTENT LIGHTING

Variations in illumination conditions (e.g. exposure and shadows) across multiple views can lead to inconsistent lighting, especially for datasets captured in real-world environments. An illustrative example from DTU Dataset is provided in Fig. 23, which demonstrates significant illumination changes between View 38 and View 40. Consequently, our method can produce incorrect decompositions in these scenes, resulting in overestimated metallic, noisy lighting, and distorted geometry near the inconsistent regions, shown in Fig. 24.

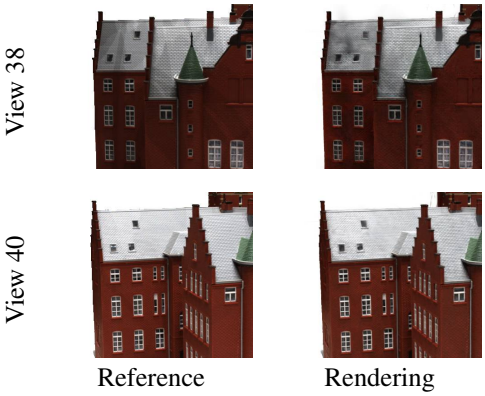

Figure 23: Inconsistent lighting on Scan 24.

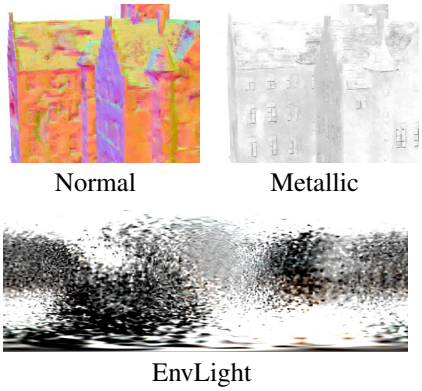

Figure 24: Incorrect decomposition.

G.3 UNDEREXPOSURE

Fig. 25 also illustrates a failure case in which the reference image is heavily underexposed. The ambiguous material-lighting composition in this scenario results in incorrect geometry recovery, as our method optimizes both aspects jointly.

Figure 25: Underexposed views from DTU Scan 110.

H MORE RESULTS

H.1 MORE RESULTS ON NERF SYNTHETIC DATASET

We provide the full table that contains 8 scenes of NeRF Synthetic Dataset in Tbl. 8, as well as more qualitative results in Fig. 26.

Figure 26: **More qualitative comparison of NVS on NeRF dataset**. Our method effectively recovers complex geometries, detailed textures, and non-Lambertian appearances, as shown in the sub-windows.

Method	Relightable	Chair	Drums	Ficus	Hotdog	Lego	Materials	Mic	Ship	Avg.
NeRF*	No	33.00	25.01	30.13	36.18	32.54	29.62	32.91	28.65	31.00
MipNeRF*	No	35.14	25.48	33.29	37.48	**35.70**	**30.71**	36.51	30.41	33.09
3DGS	No	**35.55**	**26.04**	**34.66**	**37.58**	34.63	29.63	**36.71**	**30.58**	**33.17**
TensoIR	Yes	31.45	24.40	28.51	33.55	32.20	26.74	31.59	27.78	29.53
NVdiffrec	Yes	31.66	24.31	30.01	32.67	29.01	26.84	30.22	25.64	28.79
GS-IR	Yes	29.34	23.84	28.27	32.80	33.66	25.92	30.45	27.27	28.94
R3DG	Yes	31.85	24.71	31.34	33.07	32.69	26.46	32.74	28.32	30.15
GaussianShader	Yes	33.43	25.46	33.04	35.26	33.03	28.83	34.06	28.49	31.45
Ours (stage 1)	Yes	31.98	24.53	28.96	33.85	30.83	28.43	31.32	26.23	29.52
Ours (stage 2)	Yes	**34.71**	**26.05**	**33.48**	**36.40**	**34.47**	**29.66**	**34.62**	**29.17**	**32.32**

Table 8: Detailed quantitative NVS Comparison on NeRF dataset (PSNR↑).

H.2 More Results on Synthesic4Relight Dataset

We provide all the other examples of Synthesic4Relight dataset in Fig. 27, Fig. 28 and Fig. 29. Detailed quantitative results are shown in Table 9.

Scene	Novel View Synthesis			Relighting			Albedo			Roughness
	PSNR ↑	SSIM ↑	LPIPS ↓	PSNR ↑	SSIM ↑	LPIPS ↓	PSNR ↑	SSIM ↑	LPIPS ↓	MSE ↓
Air Balloons	36.08	0.9806	0.023	30.89	0.9617	0.041	26.14	0.9215	0.068	0.018
Chair	40.92	0.9892	0.007	32.68	0.9795	0.018	29.59	0.9549	0.056	0.007
Hotdog	38.49	0.9876	0.015	27.54	0.9573	0.053	28.23	0.9572	0.087	0.037
Jugs	39.48	0.9940	0.007	35.49	0.9859	0.014	32.38	0.9732	0.040	0.005
Avg.	39.20	0.9881	0.013	31.65	0.9713	0.032	29.21	0.9517	0.063	0.017

Table 9: Detailed quantitative results of GeoSplatting on Synthetic4Relight dataset.

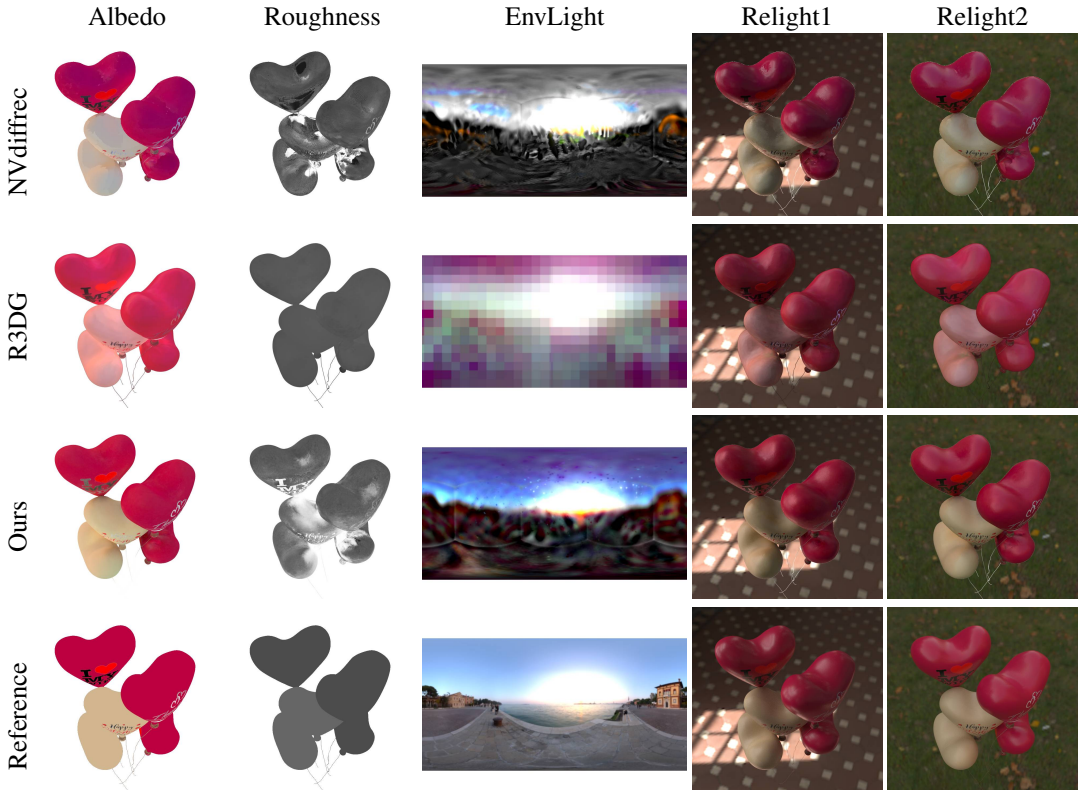

Figure 27: Qualitative comparison on Air Balloons from Synthetic4Relight dataset.

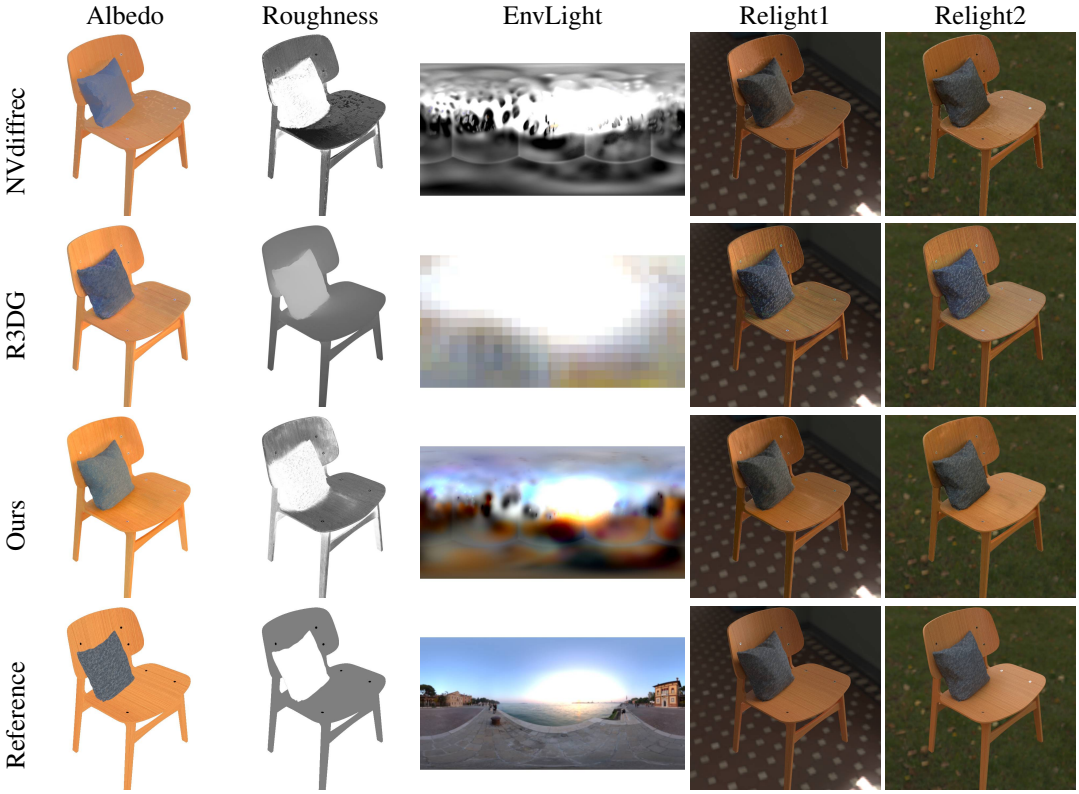

Figure 28: Qualitative comparison on Chair from Synthetic4Relight dataset.

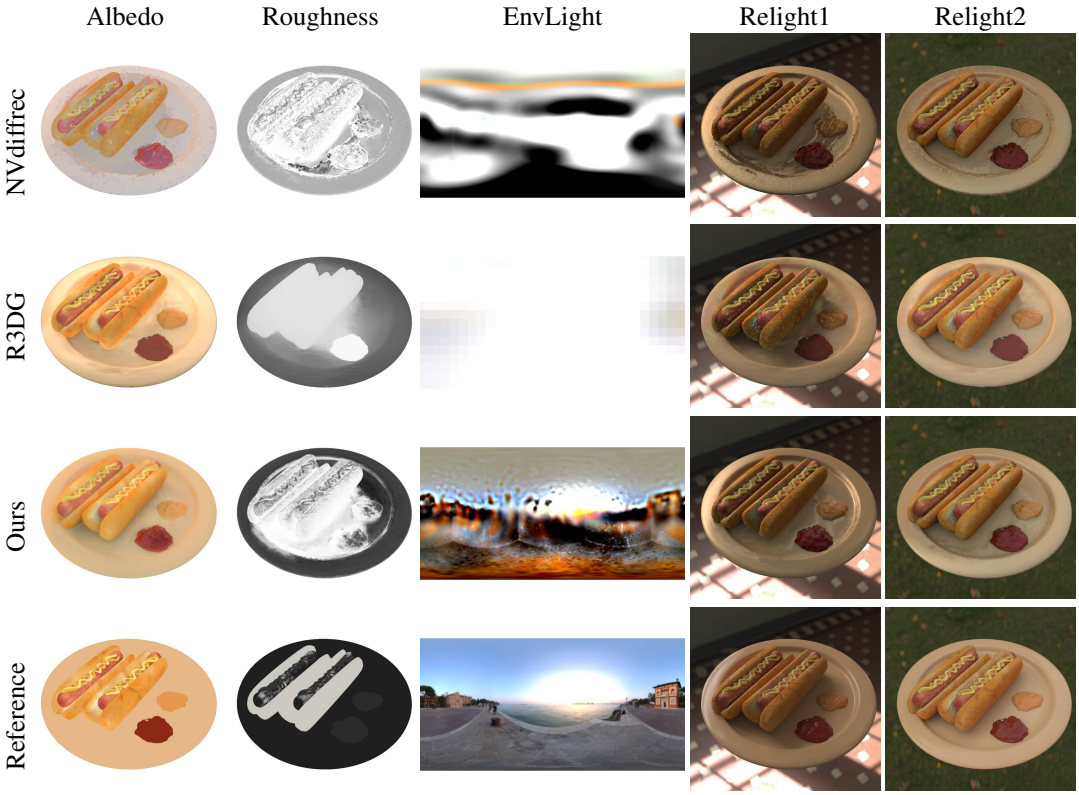

Figure 29: Qualitative comparison on Hotdog from Synthetic4Relight dataset.

H.3 Comparison on Shiny Blender Dataset

To demonstrate the inverse rendering capability for highly reflective cases, we conduct a comparison on the Shiny Blender dataset. The quantitative results are provided in Table 10 (for novel view synthesis) and Figure 11 (for normal quality). While several inverse rendering baselines, such as NVdiffrec, R3DG, and TenosIR, struggle with estimating the complex light-material interactions, resulting in degraded performance, our approach achieves the best results in both novel view synthesis and normal quality, showcasing its effectiveness in decomposing reflective objects. This is further supported by the qualitative comparison in Figures 30 and 31.

Method	PBR	Car	Ball	Helmet	Teapot	Toaster	Coffee	Avg.
3DGS*	×	27.24	27.69	28.32	**45.68**	20.99	**32.32**	30.37
R3DG	SG	27.04	23.81	26.70	42.61	20.78	32.05	28.83
TensoIR	SG	26.52	22.89	25.76	41.91	19.65	31.13	27.98
NVdiffmc*	MC	25.93	30.85	26.27	38.44	22.18	29.60	28.88
NeRO*	Split-Sum+MC	25.53	30.26	29.20	38.70	26.46	28.89	29.84
NVdiffrec	Split-Sum	24.89	21.76	27.34	40.94	23.28	30.62	28.14
GS-Shader	Split-Sum	28.41	29.64	28.46	42.51	23.22	31.62	30.64
Ours	Split-Sum	**30.58**	**42.45**	**30.51**	44.34	**26.51**	32.03	**34.41**

Table 10: **Quantitative NVS Comparison on Shiny Blender dataset (PSNR↑).** Our GeoSplatting achieves the best performance on the reflective Car, Ball, Helmet, and Toaster, whlie also significantly outperforming all baselines in terms of average PSNR. (* denotes results borrowed from the original GS-Shader paper.)

Method	PBR	Car	Ball	Helmet	Teapot	Toaster	Coffee	Avg.
R3DG	SG	4.47	16.50	5.21	0.64	9.96	5.48	7.04
TensoIR	SG	2.82	3.67	7.74	1.03	8.16	**3.13**	4.42
NVdiffrec	Split-Sum	9.35	19.91	9.29	0.88	10.76	6.08	9.38
GS-Shader	Split-Sum	3.68	5.43	14.59	2.40	8.69	7.42	7.03
Ours	Split-Sum	**1.95**	**0.39**	**3.61**	**0.50**	**6.21**	3.56	**2.70**

Table 11: **Quantitative Normal Quality Comparison on Shiny Blender dataset (MAE↓).** Our GeoSplatting achieves the best normal quality, significantly outperforming all baselines in terms of average MAE.

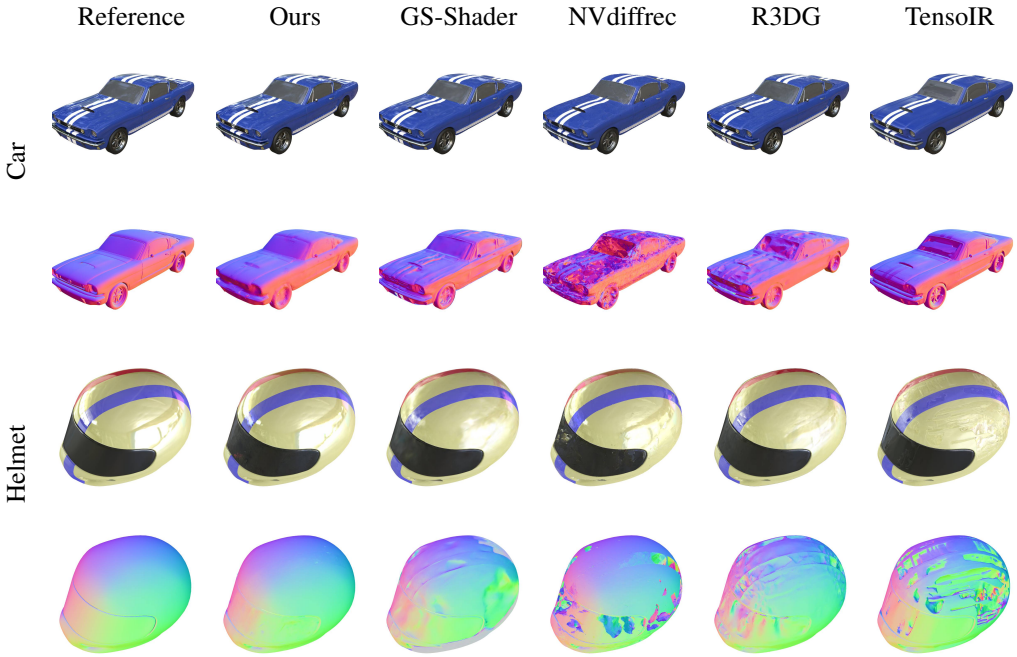

Figure 30: Qualitative Comparison on Car and Helmet from Shiny Blender dataset.

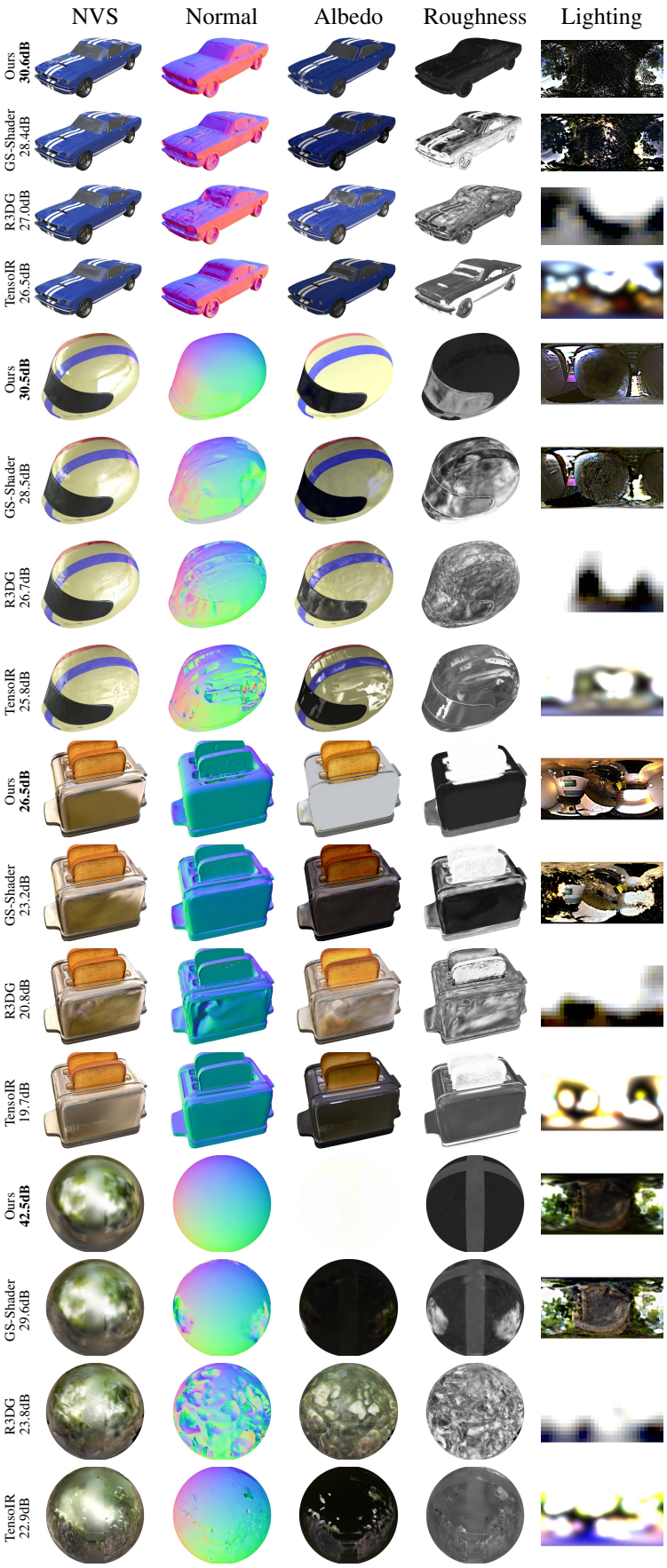

Figure 31: Qualitative Comparison of Decomposition on the Shiny Blender dataset

H.4 COMPARISON ON TENSOIR DATASET

Additionally, We perform comparison on TensoIR dataset. Qualitative results are provided in Fig. 32. Quantitative comparison are shown in Table 12. While our method outperforms existing relightable baselines in both novel view synthesis and relighting, it also achieves comparable performance in albedo reconstruction. However, we observe a decrease in albedo reconstruction quality when transitioning from Synthetic4Relight Dataset to TensoIR Dataset. This decline is primarily due to our method partially incorporating shadows into the albedo, leading to less accurate albedo for scenes with complicated occlusion (e.g. Lego from TensoIR Dataset), which presents an area for improvement in future work.

Scene	Method	Normal	Novel View Synthesis			Relighting			Albedo		
		MAE ↓	PSNR ↑	SSIM ↑	LPIPS ↓	PSNR ↑	SSIM ↑	LPIPS ↓	PSNR ↑	SSIM ↑	LPIPS ↓
Armadillo	NVdiffrec	1.998	34.31	0.986	0.025	26.59	0.925	0.050	30.51	0.953	0.068
	TensoIR	1.953	37.92	0.975	0.042	34.31	**0.975**	0.025	33.11	0.957	0.057
	GS-IR	2.650	35.44	0.962	0.040	28.93	0.922	0.083	**35.57**	0.951	0.089
	R3DG	2.479	39.54	0.981	0.032	32.44	0.951	0.068	32.89	0.954	0.076
	Ours	**1.668**	**43.68**	**0.993**	**0.005**	**34.63**	0.970	**0.024**	31.58	**0.958**	**0.042**
Ficus	NVdiffrec	3.215	27.77	0.966	0.051	23.00	0.938	0.070	25.38	0.950	0.057
	TensoIR	4.264	29.78	0.949	0.037	24.28	0.946	0.061	27.74	**0.968**	0.030
	GS-IR	5.220	20.71	0.853	0.100	25.01	0.871	0.078	29.52	0.888	0.090
	R3DG	6.493	31.99	0.975	0.027	**30.58**	0.958	0.035	**30.09**	0.959	0.030
	Ours	**2.576**	**35.45**	**0.992**	**0.006**	30.30	**0.978**	**0.016**	28.12	0.965	**0.026**
Hotdog	NVdiffrec	5.086	34.85	0.973	0.044	23.19	0.910	0.113	26.65	0.928	0.117
	TensoIR	1.953	36.69	0.976	0.022	**27.72**	0.931	0.090	26.68	0.955	0.077
	GS-IR	5.145	31.65	0.961	0.042	20.40	0.889	0.112	21.34	0.907	0.127
	R3DG	4.865	33.38	0.972	0.031	26.64	0.921	0.091	26.18	0.951	0.081
	Ours	**1.668**	**38.10**	**0.985**	**0.014**	26.07	**0.937**	**0.066**	**28.21**	**0.956**	**0.075**
Lego	NVdiffrec	9.590	31.92	0.959	0.030	25.79	0.891	0.078	20.84	0.856	0.142
	TensoIR	**5.887**	34.95	0.964	0.020	**27.71**	**0.926**	0.059	**25.86**	**0.931**	**0.072**
	GS-IR	8.608	31.72	0.940	0.036	23.05	0.853	0.089	20.76	0.823	0.159
	R3DG	8.064	30.47	0.947	0.036	24.54	0.878	0.095	25.79	0.916	0.102
	Ours	7.887	**37.07**	**0.981**	**0.011**	27.15	0.920	**0.053**	22.06	0.887	0.113
Avg.	NVdiffrec	4.972	32.21	0.971	0.037	24.64	0.916	0.078	25.84	0.922	0.096
	TensoIR	4.100	34.84	0.966	0.030	28.51	0.945	0.059	28.35	**0.953**	**0.059**
	GS-IR	5.406	29.88	0.929	0.055	24.35	0.884	0.091	26.80	0.892	0.116
	R3DG	5.476	33.84	0.968	0.031	28.55	0.927	0.072	**28.74**	0.945	0.072
	Ours	**3.874**	**38.57**	**0.988**	**0.009**	**29.54**	**0.951**	**0.040**	27.49	0.941	0.064

Table 12: Quantitative Results on the TensoIR Dataset.

Figure 32: Qualitative comparison on Armadillo from TensoIR dataset.

H.5 More Relighting on Synthetic Data

We provide more relighting results on synthetic data in Fig. 33, including Spot, Materials and Lego.

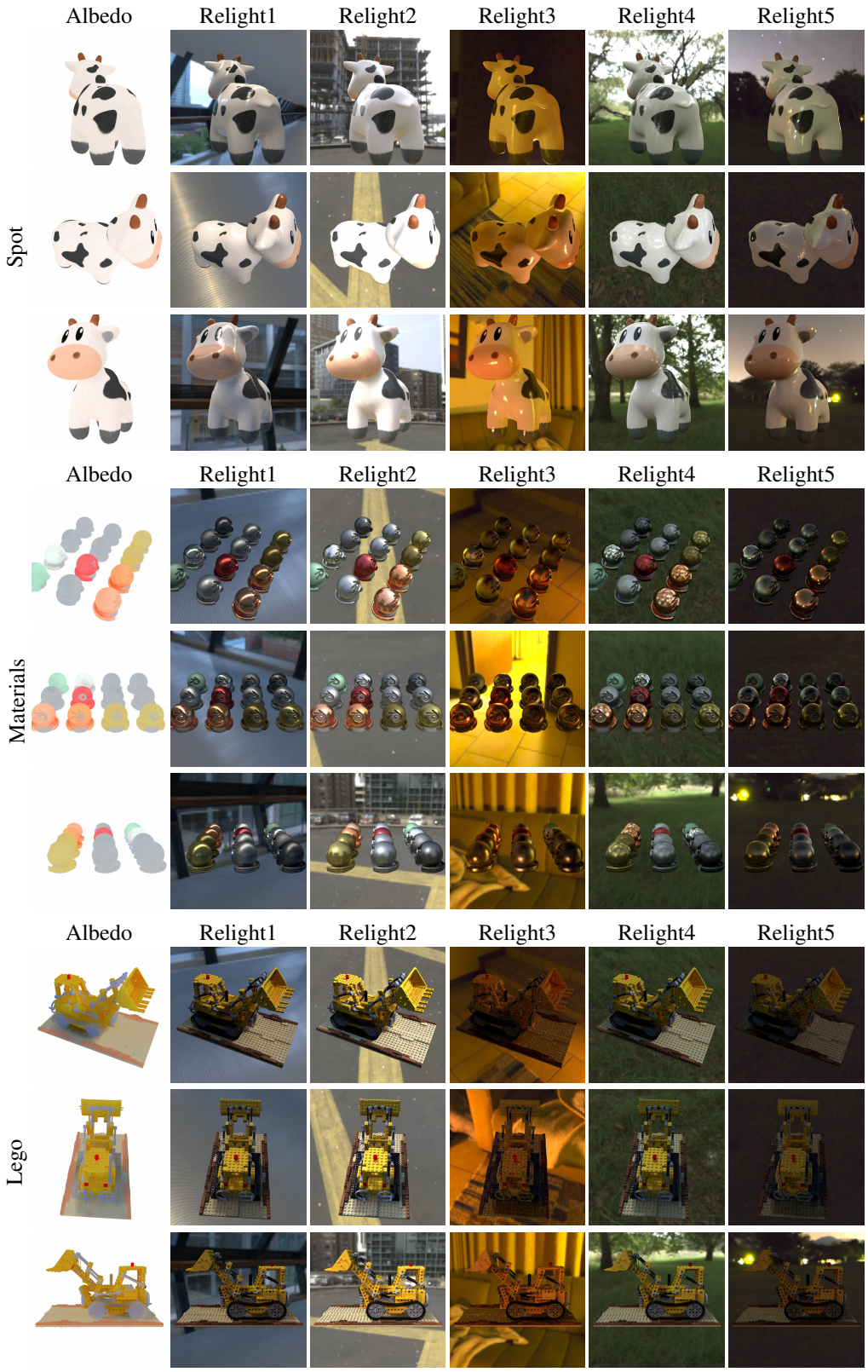

Figure 33: Relighting on synthetic data.

H.6 RELIGHTING ON DTU DATASET

In Fig. 34, we also provide real-world relighting results from DTU Dataset.

Figure 34: Relighting on DTU dataset.